Chapter 5

Calorimetry

5.1 Introduction

Most of the proposed upgrades to the CDF calorimetry are related to the Central Electromagnetic Calorimeter (CEM), one of the few remaining pieces of the original CDF detector. The CDF Central Calorimeter was baselined in 1981, before Run -2, and was designed for instantaneous luminosities of 10^{30} and integrated luminosities of 1 pb^{-1}. The demands placed on this detector by the physics analyses continually increase. The proposed upgrades are in two parts: 1) replace the slow gas detectors on the front face of the calorimeter with faster scintillator versions that have better segmentation, and 2) add timing information to both the Central and Endplug Electromagnetic calorimeters to filter out cosmic ray backgrounds.

5.2 Central Preshower Detector

5.2.1 Motivation

The CDF Central Preshower (CPR) and Central Crack (CCR) detectors will be replaced with an integrated scintillator detector. This would happen at the time the silicon detector is replaced for Run IIb. There are many reasons for this replacement: 1) The CPR is a slow wire chamber that integrates over several crossings and has relatively poor segmentation. This combination will lead to very high occupancies in Run IIb, crippling electron and photon identification. 2) Even with the modest occupancies in Run IIa, the current CPR segmentation makes it difficult to use in more sophisticated analyses such as improving jet resolutions. 3) With 10 fb^{-1} the CPR is expected to have collected 0.1 C/cm, where wire aging has typically caused significant degradation in performance, sometimes beginning with much smaller doses. 4) The thin gas layers of the CPR and CCR have much worse pulse height resolution than a scintillator detector. This is important for both electron identification and improving resolutions with a dead material correction. 5) We have an opportunity to build a much better detector for a relatively small cost. This is possible because we intend to reuse the Run IIa electronics and make use of the CDF experience in building similar detectors for the Run IIa upgrade.

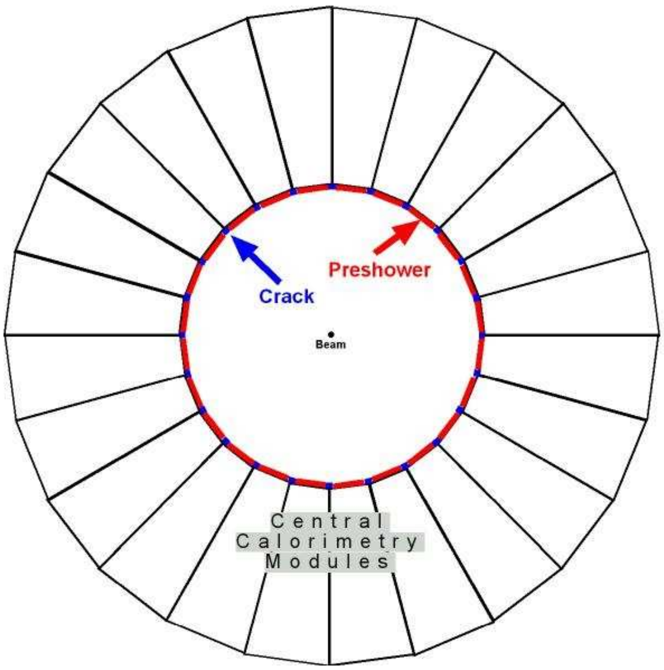

Figure 5.1: Diagram of central calorimetry wedges and the location of the preshower and crack detectors.

5.2.2 Run I Physics Using the CPR and CCR

The most important uses for preshower detectors such as the CPR are: 1) improving electron identification, 2) separating single photons from meson backgrounds, 3) improving jet resolutions for new physics searches such as the search for the Higgs. The CPR has been used extensively in electron identification in CDF. It provides about a factor of two to three more rejection of charged pions that pass all other cuts using tracking, calorimetry, and shower maximum information. This extra rejection has been crucial in soft electron ID for b jet tagging, as was shown in the first top evidence paper and displayed in Figure 5.3.

Secondly, the CPR has been used in numerous publications involving photon identification. The shower maximum detectors cannot resolve single photons from meson decays above 35 GeV since the angular separation between the two photons is too small. The CPR uses photon conversion rates which are energy independent. It was used initially to extend the QCD measurement of direct photons by more than 100 GeV in photon p_T, as shown in Figure 5.4. More recently the CPR has been used to estimate backgrounds to signals of exotic physics that include photons. New physics is expected to come at higher p_T, in a region where the shower maximum detector has no discriminatory power. It is crucial to maintain this photon identification capability for possible new signals in Run II. As the next section will show, with the luminosities possible in Run IIb, the occupancy of the current detector will be too large for photon identification.

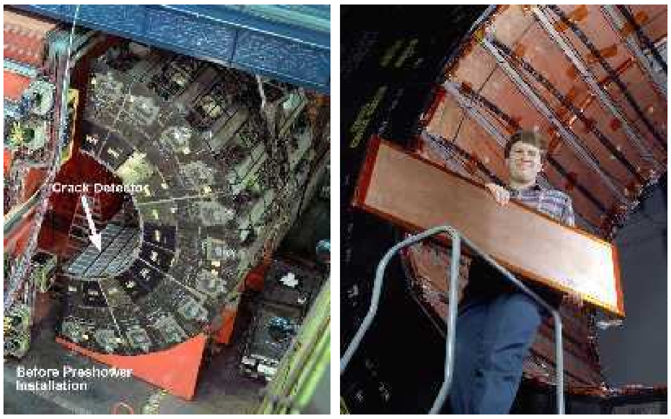

Figure 5.2: Photographs of one arch of twelve calorimetry wedges, pulled away from the beamline. The Run I preshower and crack detectors are seen lining the inner surface of the arch in the right photograph.

The use of the preshower detector to improve the energy resolution of a jet is a relatively new idea for Run II. It is well known that improving dijet mass resolution will be important in finding various new physics signals such as the Higgs, as shown in Figure 5.5. An improvement of 30% in the mass resolution (from 15% to 10%) means a factor of two less luminosity is needed to discover the Higgs. The preshower detector may help improve jet resolutions in several ways, these studies are now underway. The first way the preshower detector helps jet resolutions has already been used in Run I, in the electron b-tag in top quark events mentioned above. Due to the presence of the neutrino in these jets, CDF corrects the energy of these jets differently than those with no electron. This improves the overall energy resolution of the b jet, but no one has studied in detail precisely how much. The second way the preshower detector can help jet resolutions is by correcting for energy loss in the dead material in front of it, which the ZEUS experiment has successfully done with their scintillator-based preshower detector. We have simulated 2 GeV photons in the proposed preshower detector and found a 20% improvement in the energy resolution. Since photons provide 30% of the total jet energy, this is a 6% improvement in a jet resolution, an important contribution. A third way the preshower can help is by tagging low momentum tracks that shower in the dead material and do not escape, leaving zero energy in the calorimeter. Finally, a preshower detector can be used in other ways to improve jet resolutions in algorithms incorporating charged tracking. Since the tracking resolution is so much better than the calorimeter, the main challenge is to estimate the remaining electromagnetic (and neutral hadron) component of the jet. Charged tracks complicate this since they shower in the EM calorimeter, whereas preshower detectors can be used to estimate this contribution to the EM energy. The current CPR detector makes this difficult since a single cell spans five calorimeter towers, possibly collecting showers from other particles in the jet. A preshower detector where each cell is confined to a single calorimeter tower, such as the one in this proposal, is desirable for this purpose.

The current CDF central crack chambers (CCR) have not been directly involved in a CDF publication, but they have been checked for large pulse heights in all of the rare events CDF has observed. Their usefulness in other ways has been recently illustrated by a search for a Z peak in dielectron events, where one electron passed into a crack. Figure 5.6 shows a comparison of the Z peak measured when using the electron + track 4-vector and when one uses the electron + crack energy 4-vector. This indicates the capability of tagging high energy photons in the crack region in events which may contain new physics. The crack covers about 8% of the central detector, and in events with multiple EM objects such as the famous $ee\gamma\gamma Met$ event the possibility of one object hitting the crack is quite high. If we are lucky enough to get a sample of such events then doing measurements of this physics will require crack tagging of photons. Irrespective of the source of this single event, if SUSY is producing signals with photons as some suggest, there will be a large variety of new physics with photons and missing E_T and other objects. Crack tagging of high-energy photons will become even more important. The current crack chamber is a very thin gas layer that would be much improved with a scintillator replacement, integrated with the new preshower detector.

The CDF preshower and crack detectors are expected to play important roles in Run II physics such as soft electron tagging of b jets, photon identification in SUSY events or other new physics, and improving jet resolutions for mass bump searches such as the Higgs. The next section will explain why the CPR in particular will be severely degraded or completely useless in the high-luminosity Run IIb era.

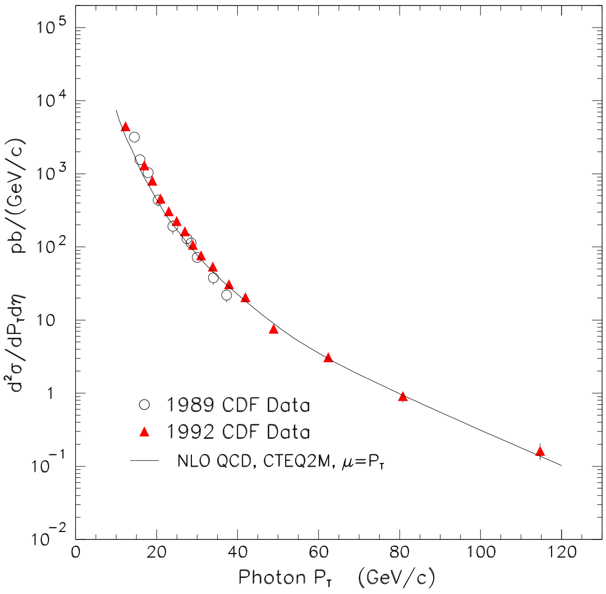

Figure 5.4: Direct photon cross section from 1989 (before CPR installation) and from 1992 using the CPR. The cross section was extended by almost 100 GeV in photon Pt.

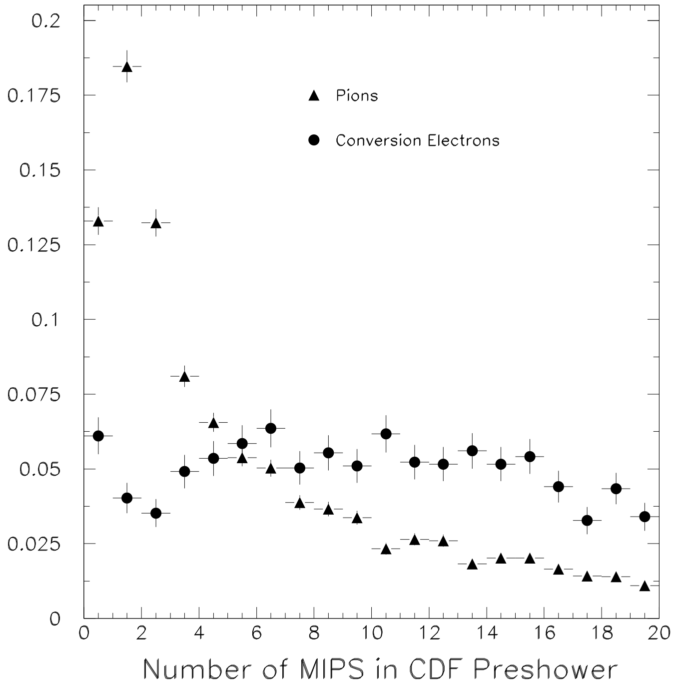

Figure 5.3: CPR response to electrons and charged pions as shown in the top "evidence" PRD.

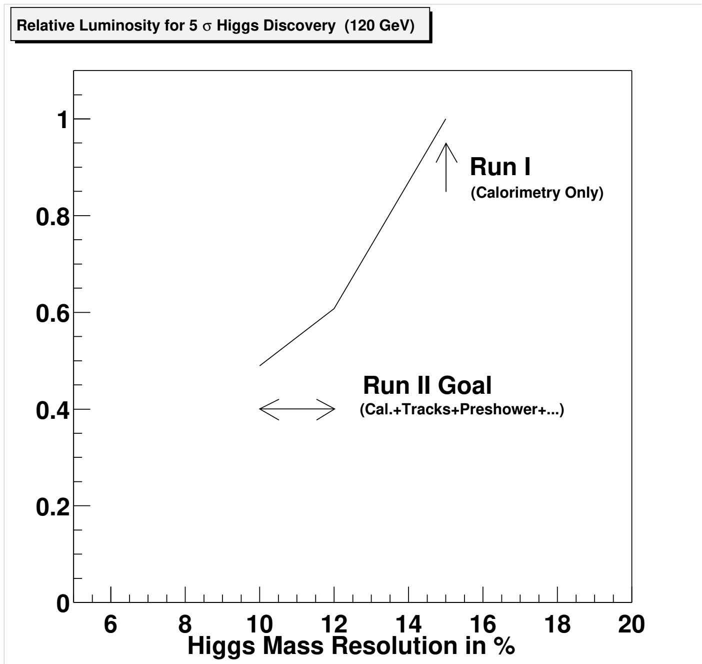

Figure 5.5: Relative improvement in luminosity needed for a Higgs Boson discovery, as a function of mass resolution.

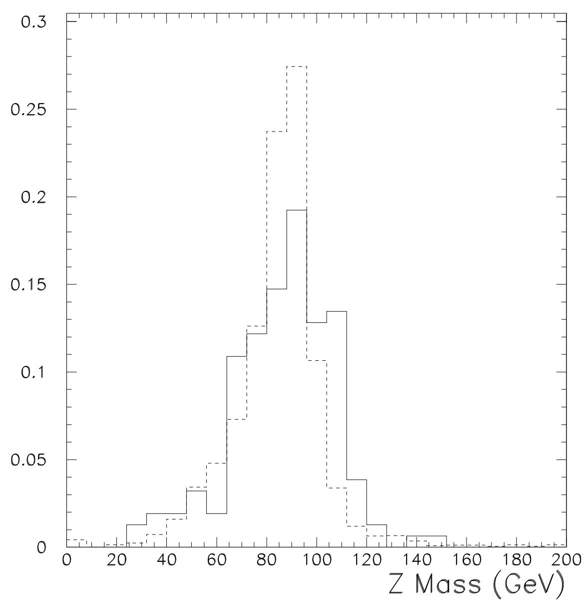

Figure 5.6: Dashed line is Z peak using electron + track, the solid line is electron plus Crack Chamber pulse height for electrons that went into the ϕ crack.

5.2.3 Occupancy Issues

The occupancy and segmentation issues discussed in this section are only relevant for the preshower detector. The current crack chambers are not sensitive to MIPS or soft photons like the CPR and the proposed crack chambers have the same segmentation as the previous ones. The CPR is a slow wire chamber and, based on early results from Run II, it appears that integrating over four crossings will be necessary to collect a significant fraction of the charge. One concrete example of a problematic scenario is if the peak Run IIb luminosities reach 6x10^{32}, with 108 bunches and 132 ns spacing. This will give rise to 5 minimum bias events per crossing. With the CPR integrating over 4 crossings, the detector will have to deal with over 20 minimum bias events! A second concrete example is the TDR situation of luminosities reaching 2x10^{32}, but with 36 bunches and 396 ns spacing. This results in 6 minimum bias events per crossing. With the CPR integrating over only two crossings in this case, a total of 12 minimum bias events are present in the CPR. With these two examples it is possible to extrapolate to any other possibility. We present Figure 5.7 as evidence of the serious difficulties the CPR could have in Run IIb. The figure shows the Run II CPR pulse height distribution in the case of overlapping 20 minimum bias events, it has an occupancy of 64%. The technique to identify photons at high p_T is to count the fraction of events in the zero bin, since single photons convert less often than multiple photons. The conversion frequency for a single photon is between 60% and 65%, so close to the background occupancy from minimum bias events that discrimination will not be possible. Similar difficulties arise for electron identification. Obviously there is a continuous degradation of performance with increasing luminosities; here we have only mapped out one possibility. But this discussion indicates that the occupancy problems in Run IIb are real. The proposed detector design will reduce the occupancy from overlapping minimum bias events by more than x10. This is accomplished by improving the detector speed with a scintillator replacement, as well as improving the detector segmentation.

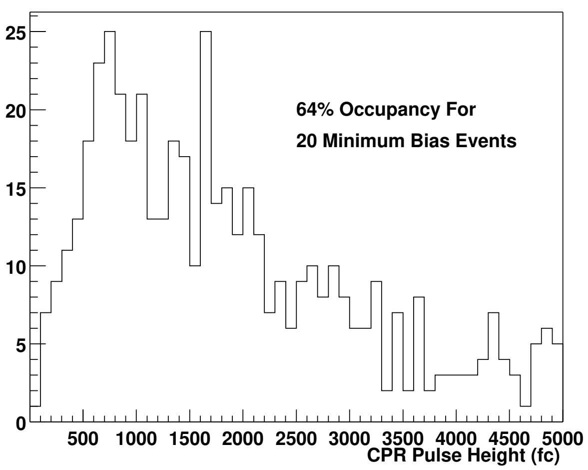

Figure 5.7: CPR run IIa pulse height for 20 overlapping minimum bias events. This background occupancy is 64%, for comparison the conversion frequency for a single photon is between 60% and 65%. The photon cross section is derived from counting the fraction in the zero bin. The occupancy of the estimated underlying event will make this very difficult.

5.2.4 Overview of Detector Design for Run IIb

The relatively limited budget available for the Run IIb upgrades necessitates a limited budget for the CPR upgrade. In this spirit, we plan to re-use the existing electronics channels currently employed in the readout of the existing CPR and CCR detectors, thus removing one of the largest components of the cost for any new detector system. At the time that the present CPR was constructed, the technology did not exist for the convenient design of a scintillator-based device to fulfill the same purpose. In the intervening years, advances in the production of wavelength-shifting (WLS) and clear plastic optical fibers have allowed for the design of scintillator detectors with WLS fiber readout with almost arbitrary segmentation and essentially complete hermeticity. Such a design has already been implemented in CDF in the plug electromagnetic and hadronic calorimeters and in the plug preshower detectors, as well as in many other experiments such as CMS and MINOS.

The new CPR will be placed in the space currently occupied by the old CPR and CCR. Figures 5.1 and 5.2 show the location of the Run I detectors in both diagrams and pictures. They cover the front face of the forty-eight central calorimetry wedges. These wedges are arranged into four "arches" of twelve wedges, which can independently be moved away from the beamline for access to the inner surface.

The new CPR should be sensitive to minimum ionizing particles (MIPS). A yield of 5 photoelectrons per MIP is sufficient for this purpose. The CCR scintillator is forced to be thinner, on the order of 6 mm, than that used for the CPR. This will result in less light but the yield should still be sufficient for the CCR functionality since it is measuring showers, not MIPs. Due to its location in the central rapidity region and at a relatively large radius, there should be little impact from radiation damage on the performance of the CPR2, even at the highest foreseen luminosities.

A radial space of 2.8 cm is available for the CPR detector and a space of 7 mm is available for the CCR. The basic design of the new CPR involves 2 cm thick scintillator tiles, segmented in η and in ϕ, as shown in Figure 5.8 along with the mechanical shell design (discussed more in the next section). The amount of scintillator needed for the new CPR is relatively modest, of the order of 50 m^2. The 2 cm scintillator has been produced by the Dubna group in CDF and is available in the quantities needed for the new CPR. The scintillator sheets will be cut into tiles and will have grooves for the WLS fibers machined in them using the facilities that are present in Lab 8 at Fermilab. Prototype tiles have been created from the Dubna scintillator using the Lab 8 tooling. The scintillator was found to be particularly easy to machine and there should be no problem with producing the required number of tiles in the timescale available.

These tiles will be read out by 1.0 mm diameter WLS fibers embedded in a roughly circular ("sigma-shaped") groove (see Figure 5.9) machined in one surface of the tile to a depth of 4 mm (and with a width of 1.5 mm). Such a groove shape maximizes the light yield and uniformity while keeping the fiber bending to a minimum. The depth of the groove allows for 3 turns of fiber to be used in order to increase the percentage of the scintillator light absorbed by the fibers; the width of the groove optimizes the combination of ease of fiber insertion and the minimization of machining of the tile. A number of commercial vendors are capable of producing quality fibers, both WLS and clear, to the specifications needed for this project. Tests are being conducted on fibers from Kuraray, Bicron and Polihitech to determine the best combination of quality and price. The fibers will be held in the groove with the use of a specially extruded polyurethane O-ring that will be placed in the groove. The O-ring will also extend 2 mm above the surface of the tile to serve as a mechanical protection for both the surface of the tile and the clear fibers.

Also, to improve the light yield, the end of the WLS fiber remaining in the tile groove will be diamond-polished and will have a thin aluminum coating sputtered onto it. The process of depositing an aluminized mirror on a polished fiber end (and then applying a protective coating) was developed for CDF and has become routine in the facility located in the Fermilab village. The tiles for each wedge will be assembled into a "tray" formed by a 2.5 mm aluminum shell. The edges of the tiles will be painted white using a titanium dioxide paint in order to optically isolate the tiles. Thin polyethylene spacers will be used to mechanically separate the tiles and to protect the paint from abrasion.

After exiting the tiles, the WLS fibers will be spliced to 1.0 mm diameter clear fibers (fibers in which no WLS dopants have been added to the polystyrene) using fiber splicing technology originally developed for the CDF plug calorimeter upgrade. Splicing to clear fibers prevents the extra light loss from the transit from the tile to the edge of the detector through WLS fibers. The splicing machines and the expertise to use them remain at Fermilab. The clear fibers will then be routed on top of the scintillator tiles to the high eta edge of each wedge, as shown in Figure 5.10, where they will be glued into a number of plastic shell optical connectors. The polyethylene spacers mentioned previously will extend approximately 1 mm above the surface of the tile and will have grooves that will organize the routing of the clear fibers. As mentioned previously, the splicing and mirroring will take place at Fermilab using Fermilab personnel. The spliced fibers will be assembled into pigtails at Michigan State University by glueing the fibers into plastic connectors and then machining the connector surface using a diamond polisher present at MSU. The plastic connectors will be precision machined in the MSU machine shop. The quality of the pigtails will be tested using an ultraviolet light scanner originally developed for pigtail production for the endplug project.

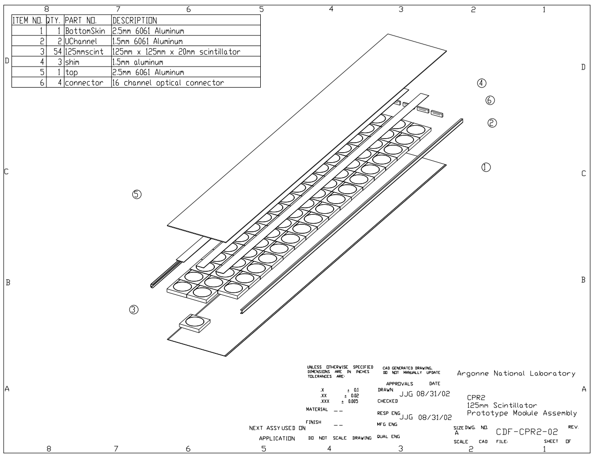

Figure 5.8: Exploded view of the current preshower upgrade design.

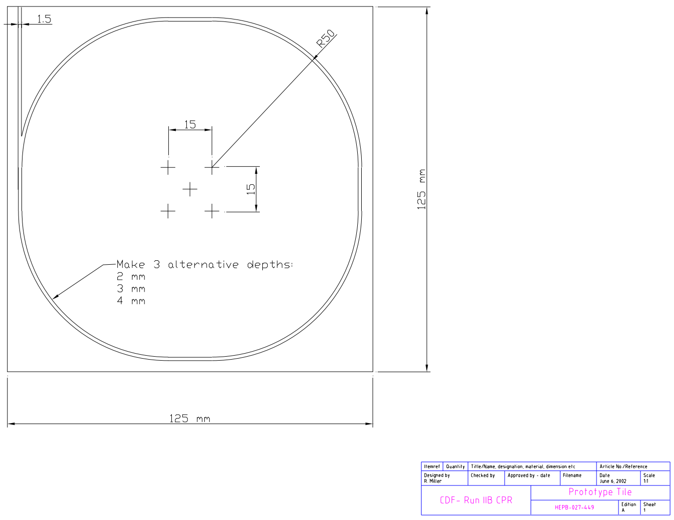

Figure 5.9: Groove cut into the scintillator tiles.

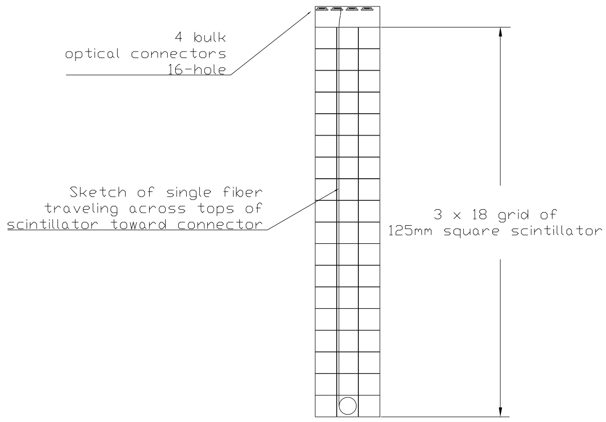

Figure 5.10: Sketch of the scintillator tile layout and fiber rout of a single fiber in the preshower detector.

Each CPR module will be enclosed in an aluminum shell that will provide both mechanical integrity and optical isolation for the detector. The current design for the shell is shown in Figure 5.12, and is relatively simple. It consists of three tiles across, 2.5 mm aluminum covers, and 1.5 mm aluminum U-channels on the end to provide support. An FEA analysis of this configuration has been performed at ANL, and a sag of 0.5 mm is expected with only a single support in the middle of the counter. We plan to support the counters in at least four locations, as the current CPR chambers are supported. In addition, a full-scale mechanical prototype has been built using fake tiles made of PVC, and deflections consistent with the FEA analysis have been measured.

An optical cable consisting of roughly 5 m of clear polystyrene fibers (1.1 mm diameter) covered by a light-tight sheath will route the light signals from the edge of the CPR through the crack to the back of each wedge of the central calorimeter. There, each optical cable will terminate in a "cookie" which will be coupled to the front surface of a MAPMT. There is a "step-up" in fiber diameter in order to reduce any effects from any possible misalignment between the pigtails and the optical cables. As for the pigtails, the connectors and cookies will be precision-machined in the MSU machine shop.

Reusing the electronics for the CPR/CCR implies two SMD cards per wedge or 64 channels. Note that modification of central SMQIE/SQUID electronics is not required. The design plan is to retain ten CCR channels and allocate the remaining 54 channels to the CPR. With this segmentation, tower-based information could be used in the optimized jet resolution algorithm.

The CCR scintillator tiles will have linear grooves machined down the center to a depth of 2 mm. As in the CPR, the WLS fibers will be spliced to clear fibers of the same diameter after leaving the tiles and the clear fibers will terminate in plastic connectors at the edge of the CCR detector. There an optical cable will transmit the light to a MAPMT at the back of the wedge. The CCR will be contained in a separate mechanical/optical structure formed from 1/32 inch aluminum.

Each MAPMT will have 16 pixels and thus will have 16 optical channels mapped to it. There will be a total of five optical cables per wedge. Three of the optical cables will have 16 CPR channels, one will have 6 CPR channels and one will have 10 CCR channels. The latter two cables will terminate in cookies that will fit together in a "jigsaw" fashion on one MAPMT.

The four 16 channel PMTs required for each wedge will be mounted in a light tight PMT box. The design of the box is shown in Fig. 5.11. The optical cable terminates in a cookie that is mounted with screws into a plate at the bottom of the box. A mu metal shield surrounds each cookie and PMT. A polarized ring aligns the PMT to the cookie and also maintains an air gap of .010 inch between the fiber ends and the face of the PMT. The PMT is held by a spring clip that is inserted into the open end of the mu metal shield. Short cables are used to collect the signals onto a 34 pin connector that will mate with 16 coaxial cable pairs. The cover, the mu metal shield, and the mating ring comprise a light baffle to make the box light tight.

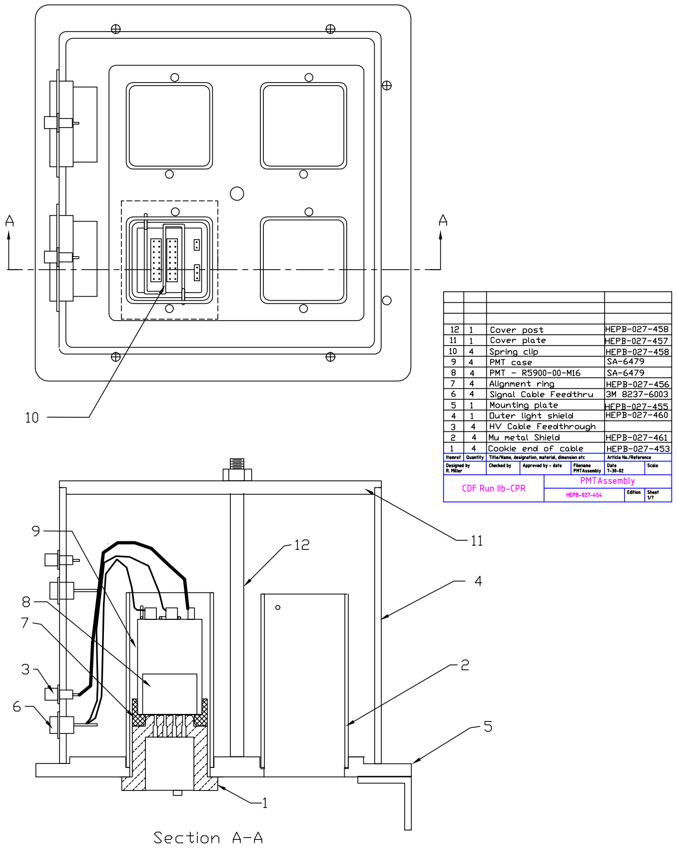

Figure 5.11: Sketch of the phototube box design.

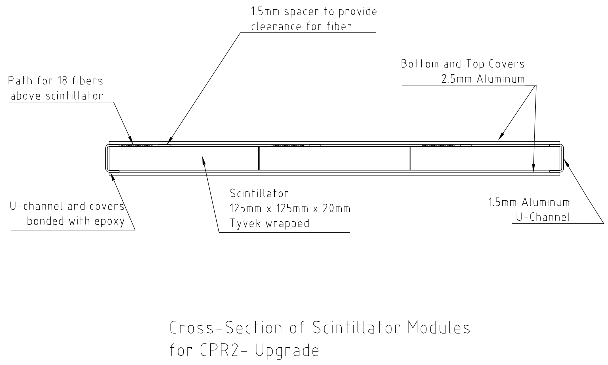

Figure 5.12: Cross section of the preshower design, showing 3 tiles across inside an aluminum shell.

5.2.5 Phototube Test Results

The readout of the detector is by the use of R5900 multi-anode PMT's (MAMPT's) manufactured by Hamamatsu. This is the same tube used for the endplug shower maximum detector. This is a 16 channel device with pixel size of 4.5X4.5 mm^2. With one detector channel per pixel, each wedge of the CPR will require 4 MAPMT's, for a total of 192 plus 10% spares for a total order of 220 MAPMT's.

We present results from a preliminary test performed at the Rockefeller University on ten Hamamatsu R-5900 MAPMT's purchased by the University of Tsukuba as part of the ongoing CPR2 R&D program. Specifications by the manufacturer are shown in Table 5.1. Individual tubes may deviate substantially from the values given by the manufacturer. It is important to measure these characteristics and verify that each tube conforms to the appropriate and acceptable ranges.

In the production run of phototubes, the University of Tsukuba will perform the task of testing the phototubes. Their teststand, utilizing two lasers, one fast and one slow, is just now being commissioned. For this reason these phototubes were tested at Rockefeller with a teststand that was used for production testing of the CDF Endplug Shower Maximum detector phototubes, as well as the CDF Miniplug phototubes.

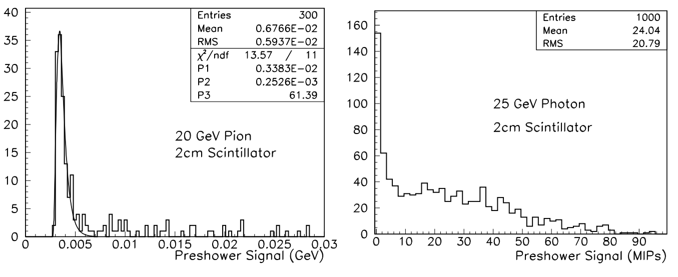

Figure 5.13: Left: the MIP signal is determined by non-interacting 20 GeV pions in the Preshower detector. Right: the Preshower response to a 25 GeV photon expressed in MIP equivalent.

In the test stand at the Rockefeller HEP Lab, we are studying the channel response uniformity, the single photoelectron response, the cross talk and the linearity, in order to optimize the voltage divider design for the CPR2 requirements. As a result of our GEANT simulation, it would be desirable to read out signals from the Preshower in the range 1-100 MIP's. Fig. 5.13 shows the MonteCarlo result for a 25 GeV photon. In the current front-end electronics, the SMQIE chip has a 13 bit dynamic range, measuring charge up to 100 pC with a resolution of 12.5 fC.

For the test we use a light sealed 'test box' which contains a light emitting diode (LED) embedded into a rectangular prism of lucite. The purpose of the lucite is to act as a 'light mixer' distributing the LED light uniformly among a set of clear fibers mounted in holes drilled in a delrin 'cookie' in a pattern matching that of the MAPMT photocathode pixels. This unit tests a single MAPMT unit at a time. The LED has been pulsed with a signal from a pulse generator at 1KHz and 50 ns wide. A couple of attenuators before reaching the LED have been used for a fine adjustment of the LED light intensity, and a light filter in front of the MAPMT has been used for the single photoelectron measurement. The testing is carried out on ten MAPMTs manufactured by Hamamatsu Corporation, divided in two groups: five (serial numbers KA2399, KA2409, KA2437, KA2440, KA2443) are a tube assembly of type H6568-MOD with an extra 17th channel, sum of the 16 channels, from the last dynode; while the remaining five (KA2402, KA2419, KA2467, KA2571, KA2633) are H6568 without dynode signal. All of them have a normal bleeder cicuit (equally divided circuit).

The uniformity of the LED light across the 4 $\times$ 4 cookie channels has been measured with three MAPMTs, and the measurement has been repeated after rotating each tube by 90°, 180° and 270°. Variations shown by these measurements are within ± 3 %.

The readout system employed for this test was a CAMAC based LeCroy 2249W 11-bit 12-channel charge integrating ADC, with a sensitivity of 0.25 pC/count, controlled by a National Instrument 'Labview' data acquisition software.

To check the reproducibility of the measurement using this setup, the output of one MAPMT was also measured repeatedly after (i) turning off/on the pulse generator which fires the LED, (ii) turning off/on the high voltage supply which powers the MAPMT, and (iii) re-mounting the MAPMT before each measurement. The variation in ADC counts is less than 1 % in cases (i) and (ii), and about $1 \sim 2$ % in case (iii).

For each MAPMT, our tests consist of a measurement of the ADC counts as a function of the variation of the input voltage, and a channel–to–channel uniformity response between the sixteen anode outputs. The MAPMT under study has a base resistor divider of $\sim 4M\Omega$. The base circuit, shown in Fig. 5.15, draws approximately 0.2 mA at 800 Volts. The maximum allowed voltage for these PMTs is 1000 Volts.

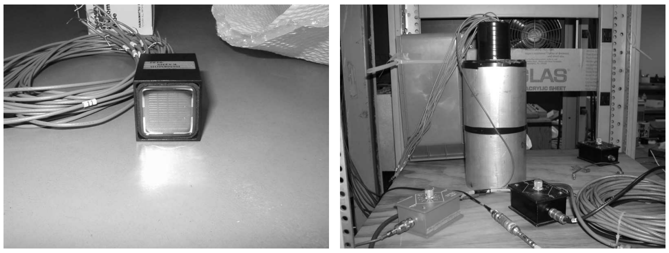

Figure 5.14: Left: The Hamamatsu R-5900 MAPMT has a 1 squared inch cross-section; Right: The test stand at the Rockefeller Lab.

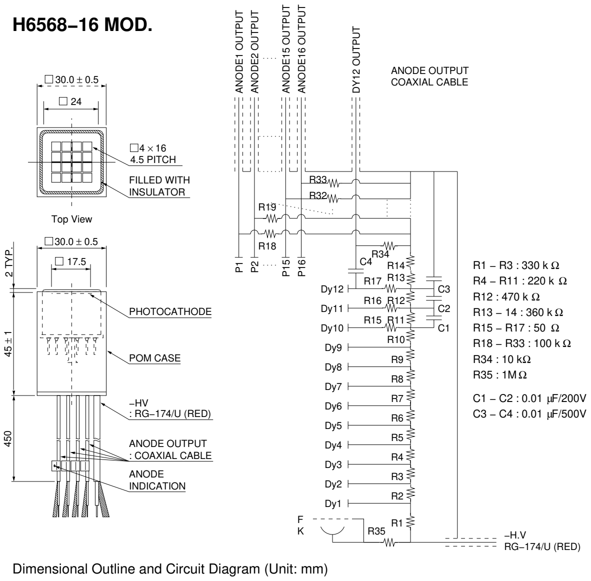

Figure 5.15: Schematic drawing of the Hamamatsu H6568-16 MOD (R5900-16) MAPMT base under study for the CPR2 detector.

A crucial issue is the uniformity of inter–pixel response. We measured the channel to channel uniformity of the ten MAPMTs under test. The channel with the highest output counts is assigned to the 100% value, and all other channels are normalized to that channel. Figure 5.16 shows the measurement for five of the ten MAPMTs tested. The dashed lines in the plot correspond to a relative variation in response between channels of a ratio 2:1. The reproducibility of our measurements is within about 5% to 10%, in the range from 600 V up to 850 V applied to the MAPMT. Figure 5.17 compares our MAPMT calibration results to the Hamamatsu specifications. For all of the ten tested MAPMT's, the two calibrations agree within ±15%.

The MAPMT's under test have a high gain, which ranges from $2 \cdot 10^5$ to $3 \cdot 10^7$ for voltages from 600V to 1000V. They have normal bleeder cicuits (equally divided circuits). We want to study the linearity of the response, as Hamamatsu also produces a "tapered bleeder" version of the base, which allows for a better pulse linearity. Use of these bleeder circuits improves pulse linearity 5 to 10 times than that obtained with normal bleeder circuits, but with a gain about ten times smaller at the same voltage.

We varied the voltage between 640V and 820V in 20 V increments, and measured the charge of the output signals. Fig. 5.18 shows a good linearity in the range 660V-760V, where most likely the detector will be operated, but deviations from linearity already start at 800V.

We also studied the single photoelectron response, by means of a combination of two attenuators before the LED and a light filter between the LED and the MAPMT.

The single-electron response can be measaured with light pulses so attenuated that the probability of each pulse giving rise to only one photoelectron is much greater than the probabilty of its giving rise to more than one.

If fluctuations in the number of photons per light pulse follows a Poisson distribution, so will the number $n_{k,i}$ of photoelectrons emitted in response to them:

$$P(n_{k,i}) = \frac{(\bar{n_{k,i}})^{n_{k,i}}}{n_{k,i}} \cdot e^{-\bar{n_{k,i}}}$$

Thus the probability of no photoelectron being emitted is $P(0) = e^{-\bar{n_{k,i}}}$; the probability of only one being emitted is $P(1) = -\bar{n_{n,k}} \cdot e^{-\bar{n_{n,k}}}$; and the probability of more than one being emitted is $P(n_{k,i} > 1) = 1 - P(0) - P(1)$. Since the ratio $P(n_{k,i} > 1)/P(1)$ tends toward $\bar{n_{k,i}}/2$ as $\bar{n_{k,i}}$ tends toward zero, it is evident that it is possible to so attenuate the light pulses that the probability of more than one photelectron being emitted per pulse is negligible compared with that of only one being emitted. In practice single-electron operation is obtained by so attenuating the

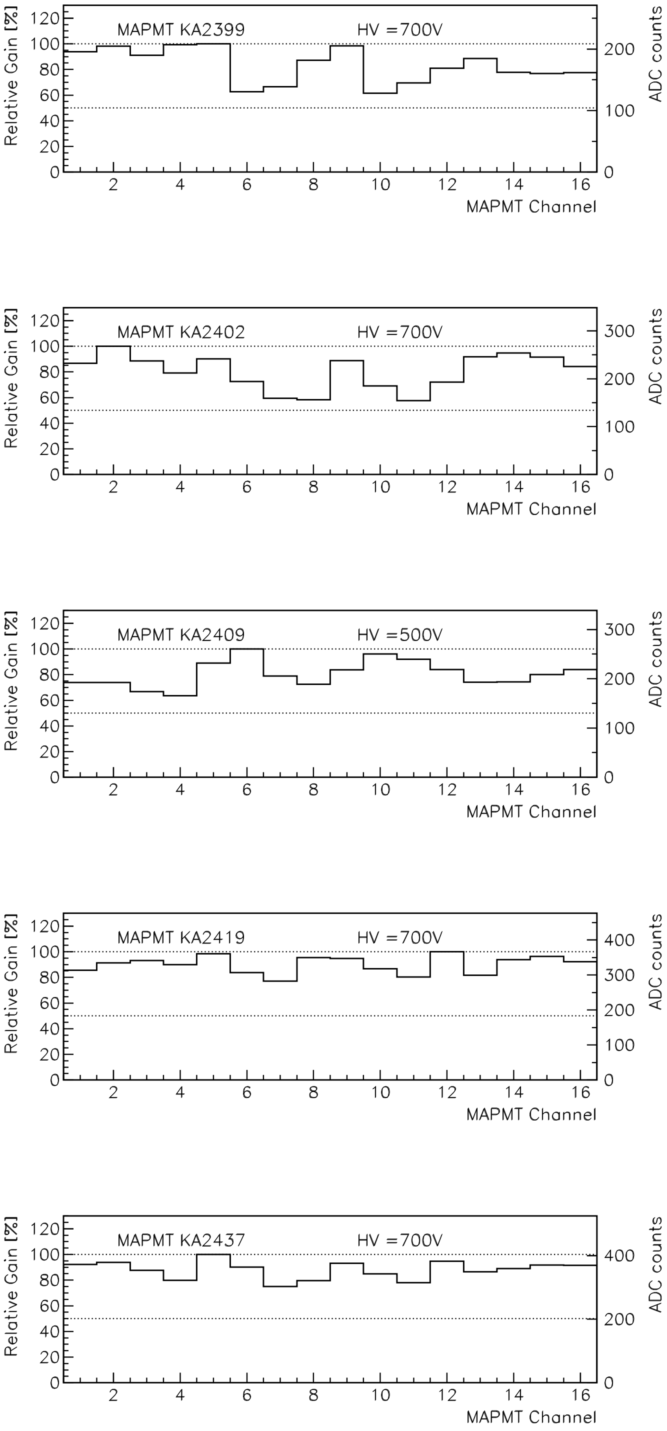

Figure 5.16: Channel–to–channel relative gain for the sixteen output signals of five of the ten MAPMTs under study. The dashed lines represent a variation in response of a ratio of 2:1.

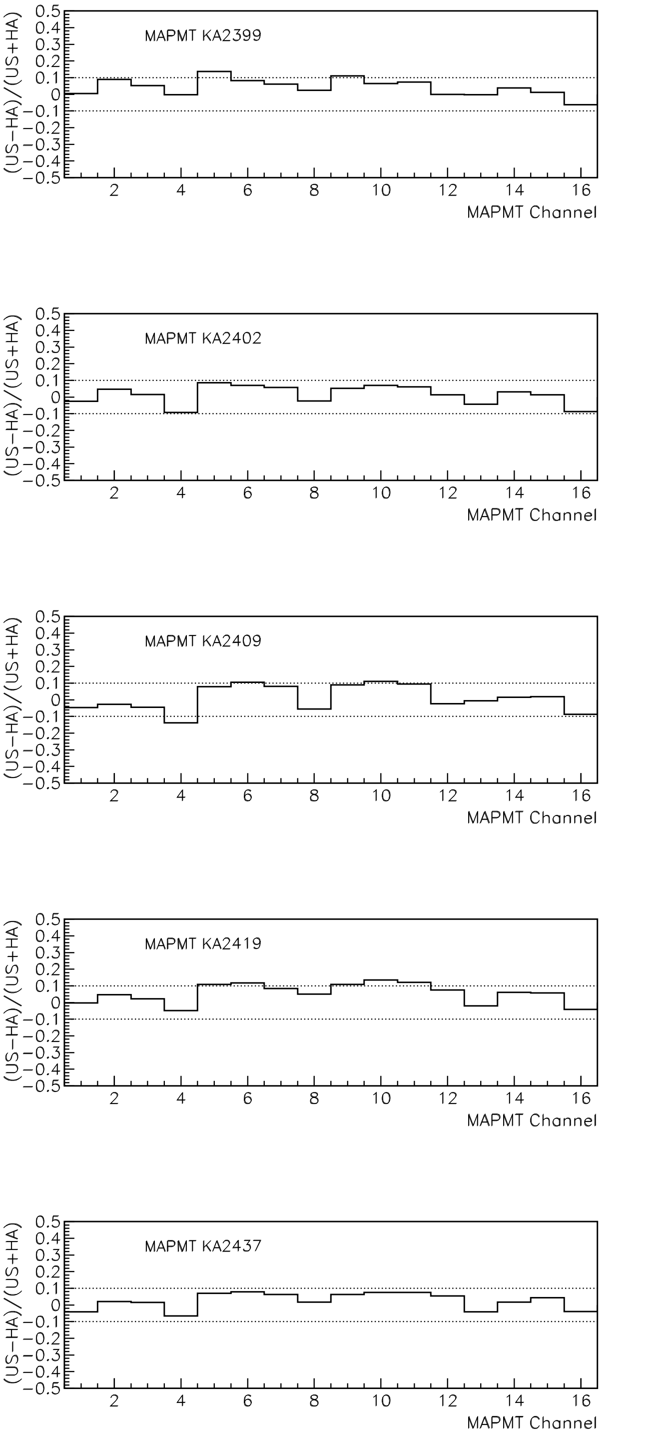

Figure 5.17: Our bench measurements (US) are compared to the Hamamatsu specifications (HA). The dashed lines in the plot correspond to a relative variation of ±10%.

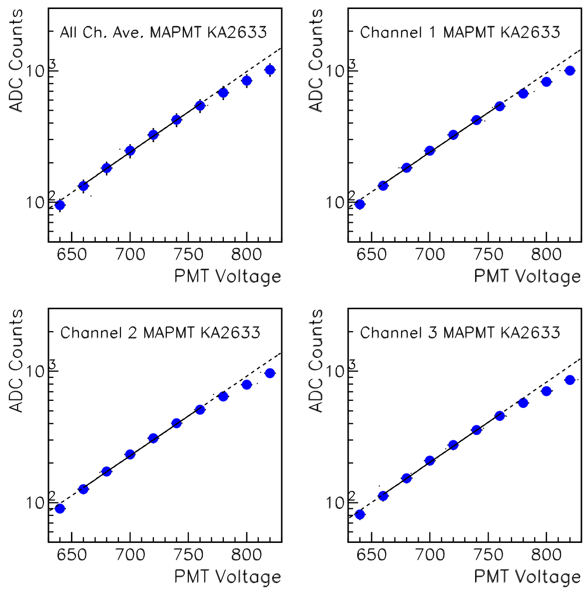

Figure 5.18: The average ADC counts are plotted as a function of the MAPMT voltage for all the channels and individually for the first three channels of the MAPMT. An exponential fit has been performed on six data points between 660V and 760V.

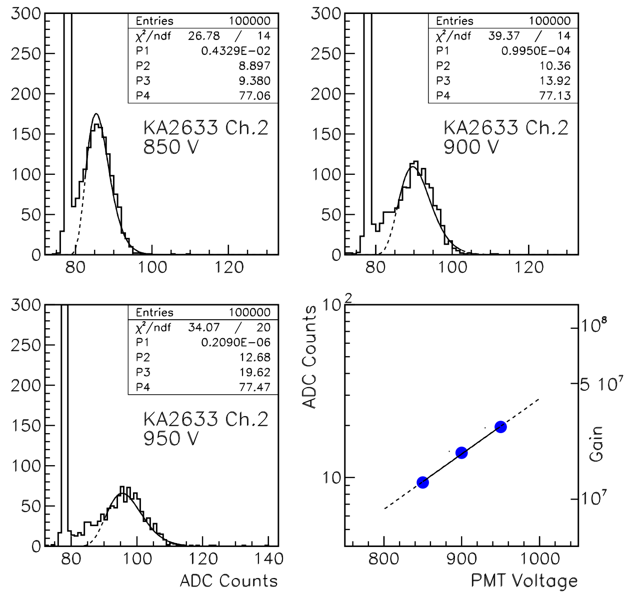

Figure 5.19: Single photoelectron response of one channel (ch. 2) of MAPMT n.KA2633 at three different voltages. The data are fitted with a *Polya distribution*, $P(m) = [m(mG/G_0)^{m-1} \cdot e^{-mG/G_0}]/\Gamma(m)$. The parameter $p3 = G_0$ corresponds to the pulse height for single photoelectrons.

light that less than one anode pulse occurs per hundred light pulses. The ratio $P(n_{k,i} > 1)/P(1)$ is then less than $5 \cdot 10^{-3}$.

Therefore the LED light in our test stand has been attenuated at the level of having less than 1,500 anode pulses out of 100,000 light pulses. In order to separate the single photoelectron peak from the pedestal, the MAPMT has been operated at high voltage/gain. Three measurements at 850V, 900V and 950V respectively, showed a linear shift of the single-photolectron peak.

The distributions in fig. 5.19 are fitted with a *Polya distribution*, i.e.

$$P(m) = \frac{m(mG/G_0)^{m-1}}{\Gamma(m)} \cdot e^{-mG/G_0}$$

which is appropriate for describing single photoelectron pulse height distributions. In the fits in fig. 5.19, $p1$ is the normalization constant, $p2$ the parameter m, $p3$ the parameter G_0, and $p4$ the pedestal mean value.

At 950V the MAPMT became somewhat noisy and the single photoelectron peak much broader.

As a cross-check of what mentioned above, fig. 5.20 shows the response of the same channel of the MAPMT n.KA2633, but now with more light resulting in a smaller (pedestal signal)/(anode signal) ratio. The contribution from two or more photoelectrons is visible in the tail of the distribution, especially at higher voltage. However, the position of the single photoelectron peak did not move much.

Cross talk studies were also performed. The cross talk deserves careful treatment as it may affect both the pattern recognition and the energy reconstruction. Analysis of this effect will provide an important gauge for MAPMT testing and calibration.

This is a two-fold effect and includes the effect of light leaking from the fibers into the neighboring channels. In addition, there is another source of cross talk from the electrons traveling down the dynodes and spuriously hitting the neighboring channels: we will call this “electronic” cross talk.

We pulse individual fibers by masking all other fibers with black tape and determine the signal leakage to the neighboring pixel in one of the MAPMT. We then rotate the MAPMT by 180 degrees relative to the light source to determine the source of the cross talk. The signal leakage is about 1.5–2.0% to each of the four neighboring pixels. This includes the

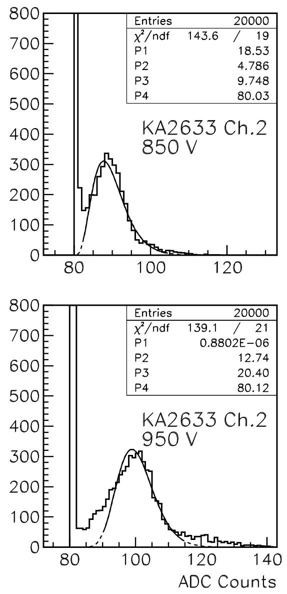

Figure 5.20: Single photoelectron response of one channel (ch. 2) of MAPMT n.KA2633 at three different voltages. With more light it is now possible to see the contribution from more than one photoelectron in the distribution tail.

Parameter	description/value
Window material	borosilicate
Quantum Efficiency	13%
Anode dark current	1 nA
Linearity	0.5 mA
Cross–talk	1%
Anode Uniformity	1:3
Photocatode material	bialkali
Spectral Response	300 to 650 nm
Number of stages	12
Anode	array of 4×4
Pixel Size	4 mm × 4 mm
Maximum High Voltage	1000 Volts
Rise time	$\leq$ 1 nsec

Table 5.1: Specifications of the R-5900 16–channel MAPMT produced by Hamamatsu.

"pedestal value" of a few counts. After we subtract the pedestals as derived from the "far–away" channels, we measure a signal leakage of about 6% into the four neighboring channels. The result does not change when we rotate the MAPMT by 180 degrees. The result is consistent with the "electronic" cross talk of $\sim$ 4% indicated in the specifications from Hamamatsu. In Table 5.1 the cross talk is $\sim$ 1% per channel.

5.2.6 Detector Prototype Test Results

Prototype modules have been constructed at both Argonne and Pisa using the 2 cm thick scintillator produced by Dubna. Grooves have been cut in eight tiles of this scintillator by Fermilab Lab 8, and a six-tile 1-tower module has been constructed and tested at ANL. The tiles were wrapped in Tyvek. In Pisa, nine tiles of a second sheet of this scintillator have been cut and grooved and tests are beginning on these as well. In neither case have the ends of the fibers been mirrored, nor have the WLS fibers been spliced to clear fibers upon exiting the tile. Therefore the current preliminary results on light yield should be considered a lower limit.

The ANL tests have used the same Cesium source mapper used for those Minos production modules built at ANL. The six tiles had 4 different configurations of groove depth and numbers of loops of fibers within the groove. All six tiles worked well in the scan, but two of the tiles were not able to be completely covered by the range of the source mapper in it's current configuration. Therefore in Figure 5.21 we present the results for the four tiles that were completely scanned. The x-axis is the source position in arbitrary units, the y-axis is a number proportional to the phototube current, corrected for relative phototube gains. The top figure shows the two tiles that had 4 mm grooves and three loops of fibers, while the bottom figure shows the two tiles that had 2 mm grooves and only one loop of fiber. The three loop tiles had a response a factor of 1.5 larger than the one loop tiles, therefore the baseline design for the preshower detector is to use three loops. Within an individual tile, a bow shape is normally seen in the response due to increased response around the fiber itself. This is very consistent with what is seen in the CDF EndPlug calorimeter. Tile 1 was a special corner tile, and the left side of its response was reduced by extra material in the corner of the module absorbing photons before detection, thereby not giving the expected bow-shaped response. Overall uniformity is quite good between tiles 3 and 4 (better than 5%), and also between tiles 1 and 2 although tile 2 has an average response 10% lower than tile 1. The cause of this is under investigation. But since tiles are easily calibrated in-situ with both cosmics and MIPs, and will be completely mapped before installation, a 10% variation among tiles is easily corrected for if it remains in the production modules.

The absolute light output from MIPs cannot be directly measured from this photon source, but an important relative determination can be made. The production Minos modules are known to produce 12 photoelectrons/MIP at the detector location where the attentuation length effects of the fibers are minimal. Immediately following the CPR tests a Minos module was mapped, and the response of this Minos module using the same teststand and phototube was 1/2 of the CPR. Since the scintillator for the CPR is twice as thick as Minos, we expect twice the current in the CPR if the response/MIP is the same between CPR and Minos. Therefore our best estimate of photoelectrons/MIP from the ANL tests is 12. Cosmic ray tests at ANL are being setup.

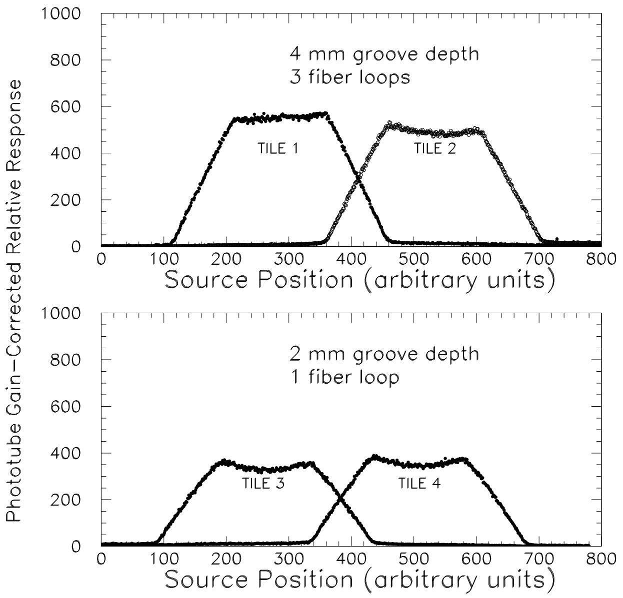

Figure 5.21: Source scan of four tiles of the 6-tile preshower prototype assembled at ANL.

The Pisa setup is a cosmic ray teststand, and the first MIP peak from a CPR prototype is shown in Figure 5.22. This was taken with a WLS fiber from PoliHiTech that was 50 cm long, and with only one loop in the tile. Optical grease was used to improve the contact between scintillator and fiber. The peak response indicates 11 photoelectrons/MIP, consistent with the ANL result but achieved in a different way. Given these results, and the fact that other known improvements to light output have not yet been implemented at either ANL or Pisa such as mirrored fibers, it seems clear that the specification of 6 photoelectrons/MIP will be easily achieved.

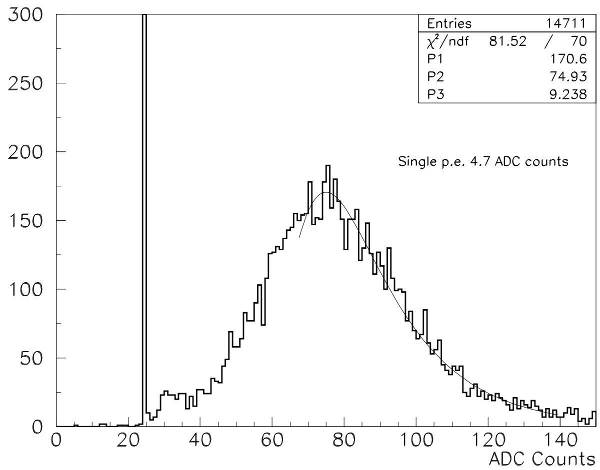

Figure 5.22: Cosmic ray MIP peak from the Pisa prototype.

5.2.7 Summary

The CDF Central Preshower and Crack detectors are playing an important role in RunII physics, and will be upgraded with a scintillator replacement to maintain and enhance its capabilities. The research and development program is well underway at four institutions in the U.S. (FNAL,ANL,MSU,Rockefeller), two institutions in Italy (Pisa and Rome), and at the University of Tsukuba in Japan. The design choices have been made to minimize cost and technical risk.

5.3 Electromagnetic Calorimeter Timing

5.3.1 Introduction

The CDF Collaboration plans to add timing information into the readout of the central and plug electromagnetic calorimeters (CEM and PEM) for Run IIb using a technique similar to the hadron TDC (HADTDC) system[1] [1, 2]. This upgrade, known as the EMTiming project, would significantly improve the potential of the CDF detector to do high-P_T searches for new physics in data samples with photons in the final state in two crucial ways:

1. It would reduce the backgrounds due to cosmic ray and beam halo sources and improve our sensitivity for important and difficult searches such as Supersymmetry (SUSY), Large Extra Dimensions (LED), anomalous couplings in $W\gamma/Z\gamma$ events etc.;

2. It would provide a vitally important handle that could confirm or deny that all the photons in unusual events, such as the $ee\gamma\gamma\not{E}_T$ candidate event [3] (see Figure 5.23) or in the CDF excess of $\ell\gamma\not{E}_T$ events [4], are from the primary interaction.

Additionally, with enough calibration data, the timing information would give us the possibility of searching for very long-lived particles which decay (1-10 nsec) into photons (for more detail see [1] and references therein).

5.3.1.1 Overview

Timing information from the calorimeter readout has been a part of the CDF detector since it was first commissioned in 1985. The HADTDC system in particular has been a powerful tool to help reject coarse backgrounds from cosmic rays and other non-primary interactions such as beam-gas or main ring splash. Adding timing information to the readout of the CEM and PEM has been suggested periodically over the years as well, but was not seen as necessary for the primary physics goals of the collaboration.

However, since the observation of the $ee\gamma\gamma\not{E}_T$ candidate event and the end of Run I, there are many new and important search channels which were not envisioned when the detector was originally built. For example, there is now an enormous amount of interest in new models of SUSY, LED, Higgs decays, and other theories which encourage searches for anomalous events with photons, and in many cases photons and $\not{E}_T$. From the earliest days of the models, and in many cases as part of their creation, CDF has played a central role. Despite the fact that the detector was not optimized for these searches, there are a number of analyses which either have been published in PRL/PRD, or will be submitted in the near future [3, 4, 5, 6, 7].

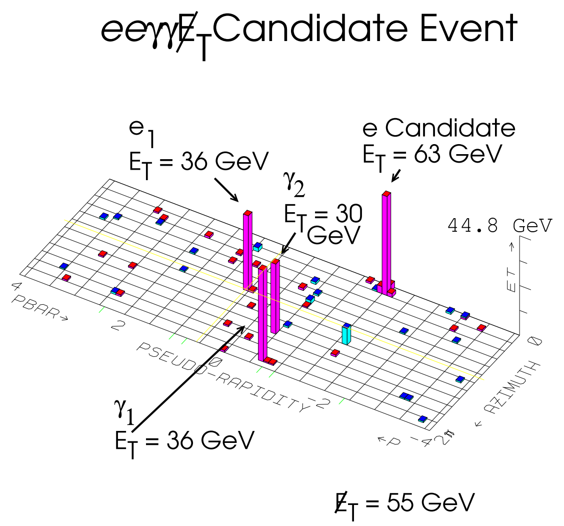

Figure 5.23: A LEGO display of the Run I CDF $ee\gamma\gamma\not{E}_T$ candidate event.

From an experimental stand point, it is now clear that timing information for each photon could play a major role in any discovery. The primary reason for this is that in each search cosmic rays or beam related backgrounds can interact with the detector and produce an additional photon and associated $\not{E}_T$ which is unrelated to the event. Timing information would go a long way to reduce these insidious backgrounds and give us a vital handle that each photon in the event is from the primary interaction. For example, in the Run I search for SUSY and LED in the $\gamma + \not{E}_T$ channel, cosmic ray backgrounds dominate all other SM backgrounds by a factor of 2 [5]. Figure 5.24 shows the E_T^γ distribution of the data and the background predictions from cosmic rays. Unfortunately, it is very difficult to reduce these backgrounds as there are striking similarity between the distribution of the identification variables for photons from real events

[1]For more information on this project please visit http://hepr8.physics.tamu.edu/hep/emtiming/

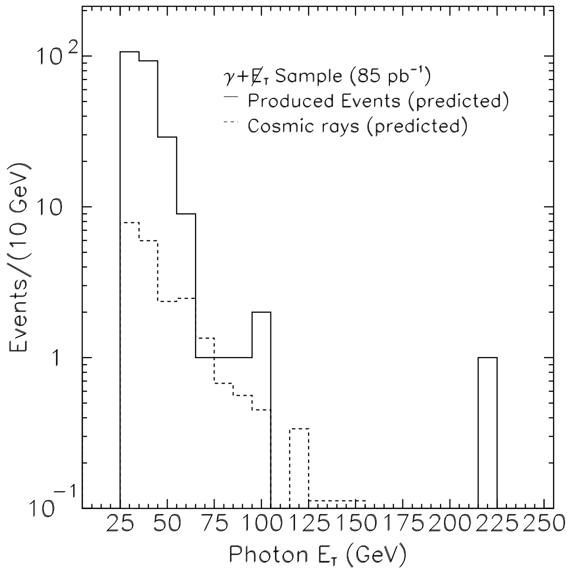

Figure 5.24: A prediction of the produced number of events in the data in 85 pb^{-1} in the $\gamma + \not\!\!E_T$ channel. Here we have folded out the HADTDC efficiency for all E_T^γ. The dashed line shows the contributions from cosmic rays.

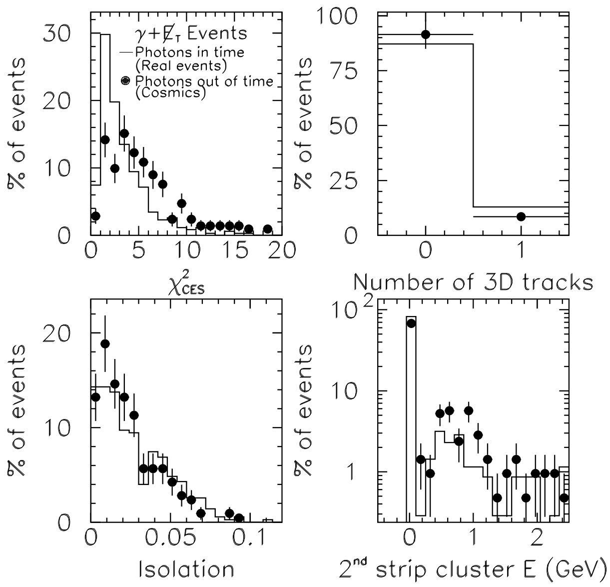

Figure 5.25: A comparison of the identification variable used to identify photons in the data from cosmic rays and from photons from the primary collision. The two distributions are largely indistinguishable.

and those from cosmic rays. See Figure 5.25. For these reasons it is clear that powerful and efficient tools are required to reject this background.

One such tool is the time of arrival of the photon relative to the collision time. In Run I, we were able to use the small amount of leakage energy into the hadronic calorimeter to fire the HADTDC system. While this method is powerful, as detailed below, it is very inefficient for low E_T photons (with a strong E_T bias) and has a bias towards more impure samples (fake photons from jets have a larger probability of depositing more energy in the HAD than prompt photons, and thus have a larger probability of firing the HADTDC system). The EMTiming project would be fully efficient for both the central and plug Run IIb and have no such biases.

A second important point is that timing information would also provide a vitally important handle that confirms that all the photons in unusual events are from a real collision. While, the CDF $ee\gamma\gamma\not\!\!E_T$ candidate event [3] and the events in the CDF $\ell\gamma\not\!\!E_T$ excess [4] are perhaps tantalizing hints of new physics; currently the detector cannot tell us if all the photons in these events are even from the primary interaction. The EMTiming project would help answer this question and would thus go a long way to improve the robustness of any potential discovery.

We begin with the physics motivation for new particle searches and the theories which predict photons in the final state. We continue with a description of why adding the EMTiming project would make a major contribution and then briefly describe the hardware, cost, schedule and manpower requirements.

5.3.2 Searching for New Physics with Photons

The primary motivation for searching in photon final states is that the photon is likely to be a good probe of new interactions, particularly SUSY. More generally, its applicability is potentially far greater as it is the only one of the three $SU(2) \times U(1)$ gauge bosons that couples to both chiralities (L and R sectors *i.e.*, V vs. $V{-}A$ or $V{+}A$) and is therefore more likely to couple to any new gauge sector. While the heavy vector bosons are also likely to couple, the photon has detection advantages over both W's and Z's as the final state particle. Photons have a better kinematic resolution and they do not suffer a sensitivity loss from branching ratios and momentum sharing between the decay products.

While final state photon searches have advantages, looking at events with photons and $\not\!\!E_T$ can have provide even greater sensitivity. There are very few standard model backgrounds which produce photons and $\not\!\!E_T$, allowing a fairly clean sample with the exception of one insidious background: cosmic rays. The bottom line is that there are a number of important and different types of searches for new physics that can be done with photons in the final state. The experimental hints from Run I, coupled with the large number of well-motivated theoretical models makes the photon final state a compelling place to look.

5.3.2.1 Theoretical Models

A large number of new physics models make a strong case that the prospects for discovery at the Fermilab Tevatron are excellent. The most well studied model is SUSY.

The two main SUSY breaking models which have recently come into favor, now predict photons in the final state. Super-gravity models [8] could produce events which decay down to neutralinos, N_2, such that the decay $N_2 \rightarrow \gamma N_1$ dominates, or $N_1 \rightarrow \gamma\tilde{G}$ [9]. In some gauge-mediated SUSY breaking models (GMSB) [8, 10, 11] all SUSY cascade decays can end in $N_1 \rightarrow \gamma\tilde{G}$, and all events have 2 photons and (some) $\not\!\!E_T$. The SUSY signals are of particular interest, as they provide a natural explanation for the $ee\gamma\gamma\not\!\!E_T$ candidate event.

Other important possibilities include:

- R-parity violating SUSY models with light gravitinos as the LSP [12];
- Grand unified theories which, for example [13], can produce heavy neutrinos which decay via $\nu_E \rightarrow \gamma n_E$;
- Composite models of quarks and leptons which, for example [14], produce excited leptons which can decay via $e^* \rightarrow e\gamma$;
- Models with new dynamics which, for example [15, 16], produce anomalous production of $W\gamma$ and $Z\gamma$ events;
- Models with LED [17] (or SUSY [18]) can predict the emission of electromagnetic radiation in Graviton or Gravitino production, respectively, producing events with the $\gamma\not\!\!E_T$ final state signature;
- Models of fermiophobic Higgs bosons [19] which can decay via $H \rightarrow \gamma\gamma$, often produced with heavy vector bosons.

5.3.2.2 Quasi-Model-Independent Searches

While there are a large number of theories that predict new particles which decay to photons, with or without $\not\!\!E_T$, a potentially far more powerful motivation is based on the idea that we have not yet correctly formulated the mechanism of electroweak symmetry breaking. This suggests that there is a good chance that the data will point the way first and perhaps the observations already noted are the first hints. There are now strong new techniques, the "cousins" methods, signature based searches and Sleuth [3, 6, 20], for making these types of exploratory searches both quantitative and systematic and we intend to use them.

5.3.2.3 Future Possibilities: Long-Lived Particles which Decay to Photons

It is possible that with enough time and calibration data ($W \rightarrow e\nu$) the system would allow for a new class of searches for long-lived particles which decay to photons. In a GMSB scenario where $\tilde{G}$ and N_1 are the LSP and NLSP, the $\tilde{G}$ mass is expected to be in the range between 1 eV/c^2 and 10^4 eV/c^2 [11]. This can lead to an N_1 which can decay via $N_1 \rightarrow \gamma\tilde{G}$ with lifetimes of order (1-10 nsec). If we can calibrate the timing to be ≈1 nsec, the system should be powerful enough to study this class of models. The current HADTDC system has approximately 4 nsec of timing resolution [21]. The resolution possibilities are still under study [22]. The issues of how efficiently the photon identification will do with photons which originate from a displaced vertex will also have to be studied.

5.3.2.4 Physics Summary

To summarize, there is a compelling case to do physics with photons in the final state, and the EMTiming project would play a central role in reducing cosmic ray background and enhancing the robustness of any potential signal. Any set of Tevatron searches (SUSY, Higgs, LED etc.), must contain the $\gamma\not\!\!E_T + X$, $\ell\gamma\not\!\!E_T + X$, $\gamma b\not\!\!E_T + X$, and $\gamma\gamma\not\!\!E_T + X$ channels where the photons are promptly produced and vulnerable to experimental problems. In addition we expect that the robustness of the charged lepton channels of measurements of SM $W\gamma/Z\gamma$ will be enhanced by the EMTiming system. New channels such as $Z\gamma$ in the $\nu\nu\gamma$ channel may potentially open. Perhaps with enough calibration data we can even search for long-lived particles that decay to photons.

5.3.3 The EMTiming Project

The EMTiming upgrade is similar to the HADTDC system in that both use the same hardware designs to record the time of arrival of any energy deposited in the EM and HAD calorimeters respectively. In Run I, the HADTDC system was used to find the 'timing' of those few photon candidates which have energy "leakage" out of the CEM and into the CHA [23]. This method is very powerful in separating backgrounds. Figure 5.26 shows a comparison of the timing in the HADTDC's for promptly produced particles and for cosmic rays. As shown in the figure, prompt particles have a distribution which is centered at the time of flight from the collision point to the calorimeter with a resolution of a few nsec. Cosmic rays are spread evenly as a function of time. Rejection of cosmic ray backgrounds using timing in the calorimeter clearly has excellent rejection power, and allows for a straight forward method of background estimation.

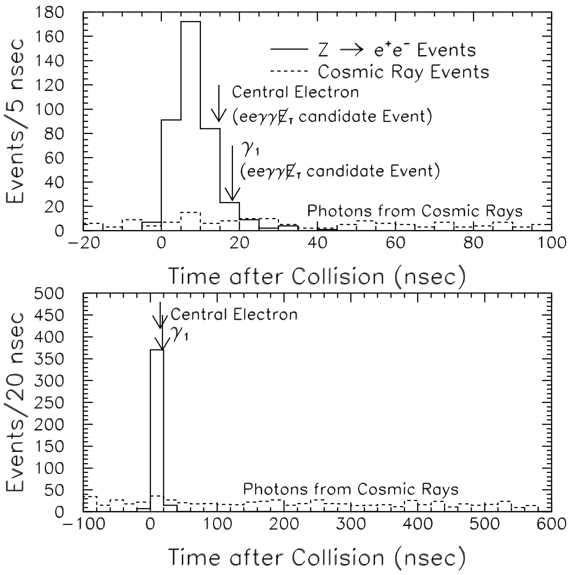

Figure 5.26: A comparison of the timing information for electrons from $Z \to ee$ and cosmic rays events using the central hadron calorimeter in Run I. Note that for true electrons the distribution is centered at the time of flight from the collision point to the calorimeter and that the unoptimized resolution is a few nsec. Cosmic rays are spread evenly as a function of time as expected. The arrows indicate the timing of two of the four EM clusters in the CDF $ee\gamma\gamma\not\!\!E_T$ candidate event. Only three of the four were in the central part of the calorimeter, and only two deposited enough energy to fire the HADTDC's with the photon just barely above threshold.

Unfortunately, even though many photons deposit some energy in the HAD, the efficiency of getting timing information is often not high. Figure 5.27 shows that the inefficiency in Run I is a strong function of the E_T of the photon; it has an efficiency of roughly 20% for $E_T^\gamma = 20$ GeV and a plateau around 100% above about 80 GeV, and was only instrumented for the central calorimeter. In Run II the PHA calorimeter is also instrumented and preliminary results for Run II are shown in Figure 5.28. Both CHA and PHA show an improvement over Run I as the central TDC energy threshold is lower, and the plug is now instrumented. However, the noise/activity in the plug requires a higher leakage energy threshold and has a larger inefficiency than the central for small E_T. In contrast, we expect that the EMTiming system would be fully efficient for all useful photon energies for both small and large η.

While the timing from the HADTDC system is clearly beneficial, the inefficiency is deadly in many standard analyses. To illustrate this, Figure 5.29 shows the kinematics from an ensemble of two photon events from Gauge Mediated SUSY model. The two curves in Figure 5.29 compare the expected number of timed events using the EMTiming and HADTDC timing (using Run I numbers) systems. From the figure, it is clear that it would not be a robust search technique to require all photon candidates in every $\gamma\gamma\not\!\!E_T$ event be timed using the HADTDC system. However, to make a numeric comparison, we note that the event yield would be doubled by the EMTiming system.

Another useful way to benchmark the additional sensitivity of the EMTiming system is to compare the event yield of standard model production of $Z(\to \nu\nu)\gamma \to \gamma + \not\!\!E_T$ events with and without the system. Results from SUSY and LED, modulo production cross sections and differences in mass scales, are comparable. Figure 5.30 compares the expected yield of timed events from the EM and HAD calorimeters for the central detector only (where the HADTDC system is most efficient). The mean photon energy lies in the region of low HADTDC efficiency and is falling exponentially. In the Run I $\gamma + \not\!\!E_T$ analysis [5], in order to make a robust search the E_T^γ thresholds were raised to 55 GeV where the HADTDC system is almost fully efficient. With the

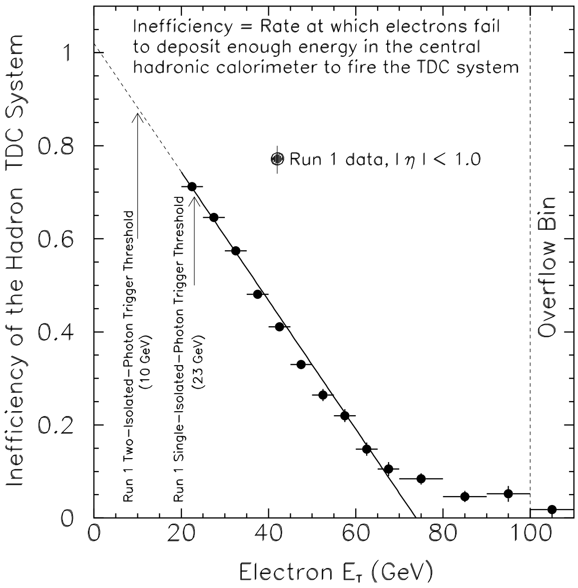

Figure 5.27: Inefficiency for electrons to have enough energy deposited in the hadronic calorimeter to fire the TDC's and be within the timing window for Run I. We assume that the efficiency for electrons and photons are equal since their shower characteristics are similar for the amount of energy deposition in the HAD. Note that the region to the right of the vertical dashed line is all events above 100 GeV.

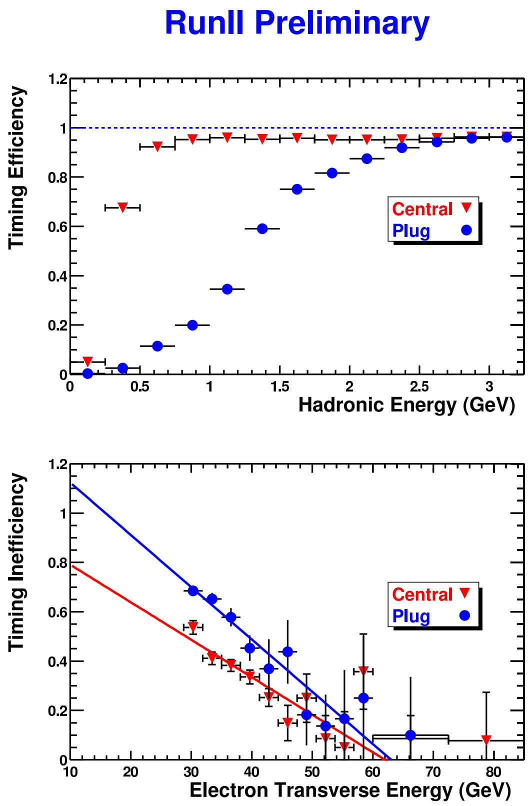

Figure 5.28: The Run II HADTDC timing efficiency. The top plot shows the efficiency to fire as a function of deposited energy in the CHA and PHA respectively. The bottom plot shows the inefficiency for electrons to have enough energy deposited in the hadronic calorimeter to fire the TDC's.

EMTiming system, we would be fully efficient for all events which pass the $\gamma + \not\!\!E_T$ trigger thresholds of 25 GeV each. Comparing the predictions above 55 GeV and above 25 GeV, we expect a factor of 30 improvement in event yield. Perhaps with enough data, we could do a measurement of $\bar{p}p \to Z(\to \nu\bar{\nu}) + \gamma + X$ in Run IIb. This process has the advantage over the $\ell^+\ell^-\gamma$ channel by a factor of 3 in the branching ratio, and almost a factor of 2 in the acceptance. We note that DØ , which has a pointing calorimeter and has no such problems with cosmic ray backgrounds, has produced the dominant $Z\gamma$ measurement to date from the Tevatron by using the $\gamma\not\!\!E_T$ channel [24].

Using a SUSY scenario of $\tilde{G}\tilde{G}\gamma$ production, we estimate that the EMTiming system, and just lowering the threholds to 50 GeV, would improve the cross section limits in the $\gamma + \not\!\!E_T$ analysis by a factor of two over the HADTDC system alone. This improvement should improve the limits on $\sqrt{F}$ by 20 GeV. See Figure 5.31. Further improvements are possible, but will require a new analysis to reduce the next-most dominant backgrounds which were not previously considered.

5.3.3.1 Tell-tale Handles in Important Events

The efficiency loss in using the HADTDC's to do *a priori* photon physics searches is disappointing. However, *a posteriori* this inefficiency could undermine a potential discovery or cause an embarrassing mirage. The pressing nature of having a high efficiency timing measurement is illustrated in Figure 5.26 which also contains the timing for the two electron and two photon candidates in the $ee\gamma\gamma\not\!\!E_T$ candidate event. Three of the four objects were in the central calorimeter and the other in the plug. *A priori*, from the kinematics of the two photon and electron candidates, we expected 1.4 of them to fire the HADTDC system (there was no timing in the plug so there was no possibility for the PEM cluster). The data fluctuated in our favor and two of the four deposited enough energy in the HAD to fire the

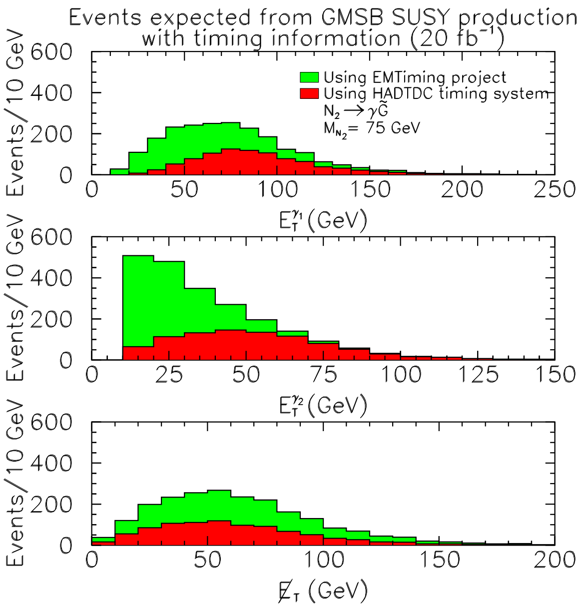

Figure 5.29: Histograms of the distributions of photon E_T and $\not{E}_T$ in a gauge-mediated model of SUSY [3]. The light shaded histogram shows the predicted signal with timing information available in electromagnetic calorimeters. The dark shaded histogram shows the predicted signal with no timing available from EM calorimeters.

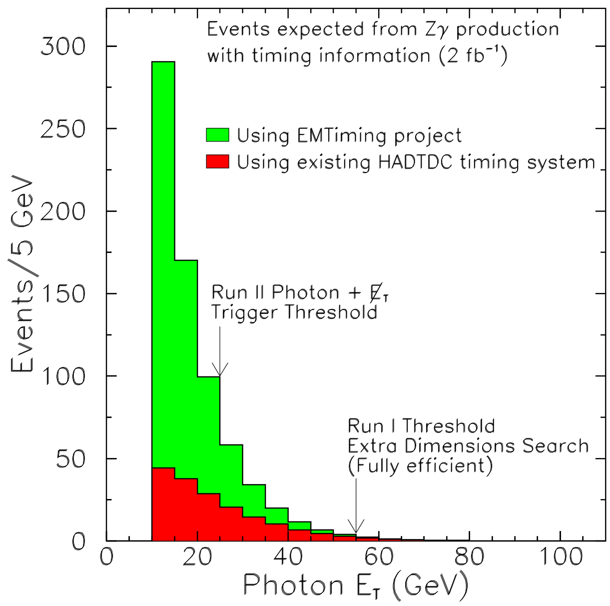

Figure 5.30: The prediction for the photon E_T spectrum from $Z\gamma$ events. The light and dark shaded curves shows the expected yield of timed events from the EMTiming and HADTDC systems in Run II. Note that the Run I $\gamma + \not{E}_T$ analysis required a photon E_T of 55 GeV. The $\gamma + \not{E}_T$ trigger threshold is at 22 GeV and reducing the kinematic requirement would increase the event yield by a factor of 30. One can also see that number of photons which would be timed from $Z\gamma \to \ell\ell\gamma$ which come in on the leptonic triggers would be even larger.

TDC's. We note that the photon was barely above threshold. The fact that both the electron and one photon are in time is actually quite an interesting result as it helps confirm that at least part of the event is from the primary collision. For Run II, even with the PHA timing, the efficiency of the plug is low (again see Figure 5.28) and the probability of tagging all four clusters is of the order of 5% as compared to the ≈100% for EMTiming.

The cosmic ray contamination to diboson events ($W\gamma/Z\gamma$) in the charged lepton decay modes is expected to be small, but can cause large disruptions. For many years, electroweak measurements of anomalous couplings in diboson production have been seen as fairly robust since the charged lepton has a strong handle from the tracking chamber. However, the recent CDF excess in the $\ell\gamma\not{E}_T$ channel has called this into question [4]. There is a serious worry that since the photon and any $\not{E}_T$ have no timing handle that the events are vulnerable to errors which affect both the counting experiments and the kinematic distributions. For example, a $W \to e\nu$ event with a cosmic ray would look like a $W\gamma$ event with anomalous $\not{E}_T$, and while the background estimates indicate that the contribution from cosmics is small, only about half of the photon events in the $\ell\gamma\not{E}_T$ sample had timing information in them. Similar problems could occur in $Z \to ee$ events. An overlapping cosmic ray would give an $ee\gamma\not{E}_T$ signature, which has no significant direct SM backgrounds. Similarly, and perhaps more interestingly, with the large number of $W\gamma$ and $Z\gamma$ events expected in Run II, the possibility of observing a fake $e\gamma\gamma\not{E}_T$ event becomes daunting.

Using the HADTDC readout to infer that a photon is part of the primary collision also has systematic problems. For example, since the timing is based on the hadronic energy deposited, there is a bias toward photons which have more hadronic energy associated with it i.e., more likely to be a fake from a jet. A second more difficult problem, is that since it only takes a small amount of energy in the HAD to fire the TDC system (approx 50% efficient at 0.5 GeV), hadrons from the underlying event can cause the system to fire even if the primary photon does not. Thus, even in the $ee\gamma\gamma\not{E}_T$ candidate event the photon for which there is HADTDC timing information (γ_1 in

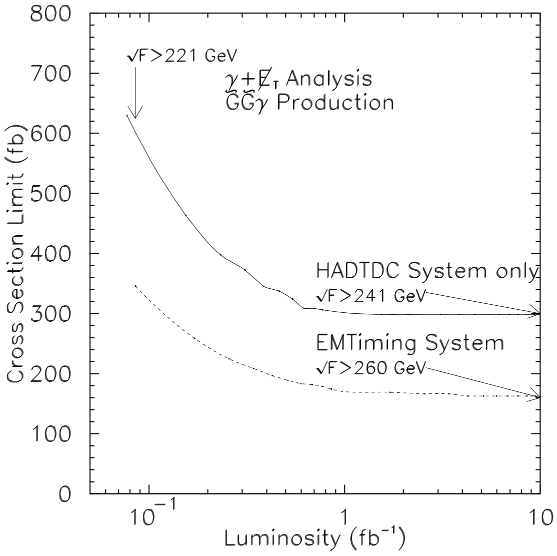

Figure 5.31: A comparison of the expected 95% C.L. limit on $\tilde{G}\tilde{G}\gamma$ production in the $\gamma + \not\!\!E_T$ channel using the HADTDC and EMTiming systems.

Figure 5.26), there is a finite probability that the photon is in fact out of time, but appears in time because energy from the underlying event fired the TDC. Preliminary studies suggest that about 5% of the time a cosmic ray which is out of time with the collision will have underlying event which will deposit enough energy in the HAD to fire the TDC system. The EMTiming system would be far less sensitive to such problems since we are firing directly on the large amount of energy deposited, and we can tune the threshold to be in the few GeV range.

While there are estimates as to the rate at which cosmics can contribute photons to an already existing event (and such estimates appear to be negligible [3]), it is clear that statistics are a worry in a sample of a few events, and an even greater worry in a sample of one event. Direct timing for both the CEM and PEM are, and would have been, of great benefit in these two important instances. We will never know if these events are due to an overlap. It is certainly possible that this type of problem could occur in the future and the EMTiming system would allow for all photon candidates (in both central and plug, for large and small E_T) to have the necessary timing information to negate this effect

5.3.4 Hardware, Cost, Schedule and Manpower

The hardware for this system is designed to mimic that of the hadron calorimeter TDC system as much as possible. However, we have made a small number of changes in an effort to minimize both the cost and the risk by making the entire system connectorized. This would allow us to recreate the the existing system and put it back exactly as it is today with minimal effort. Since there is no new technology in this design, we have not supplied a great deal of technical detail in this summary. More details can be found in Refs. [1, 2]. The path, which is illustrated in Figure 5.32, is:

$$\text{PMT/Base} \stackrel{\text{Cable}}{\longrightarrow} \text{Transition Board} \stackrel{\text{VME Backplane}}{\longrightarrow} \text{ASD} \stackrel{\text{Cable}}{\longrightarrow} \text{TDC} \stackrel{\text{VME}}{\longrightarrow} \text{Readout}$$

In this system the signal comes out from the phototube and collected with the tubes from the rest of the wedge on a transition board which is on the backside of a calorimeter readout VME crate. All the lines are passed through the VME backplane into an Amplifier Shaper Discriminator (ASD) which effectively turns the signal into an LVDS digital pulse suitable for use by a TDC. The signal is sent out of the front panel of the ASD, and upstairs to a TDC which is then readout into the event. Figures 5.33 and 5.34 show the individual components used in the CEM and PEM respectively.

Currently there are 960 CEM phototubes, none of which have a base that is compatible with readout for timing. To remedy this we are using a custom splitter to the CEM output [25] using low-cost, off-the-shelf components. The splitter itself is a fully passive element designed to be completely connectorized so that it may easily installed (or de-installed if necessary) in the system. Currently the CEM phototubes are readout using custom bases which have the anode connected to a 25' RG174 cable via a LEMO connector. The other end of this cable is soldered directly onto a transition board which is attached to the ADMEM system which integrates the charge to give a full energy measurement. The splitter is designed to be inserted directly into the PMT base, have the original LEMO/PMT end of the ADMEM line go to the primary output of the splitter (using a female LEMO connector on the splitter), and have the secondary (split) line go to an ASD transition

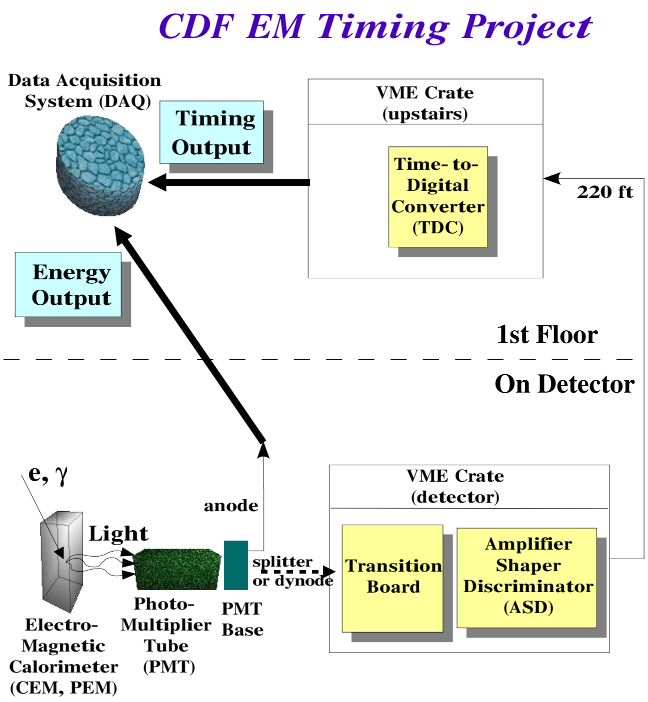

Figure 5.32: Layout of the EMTiming project.

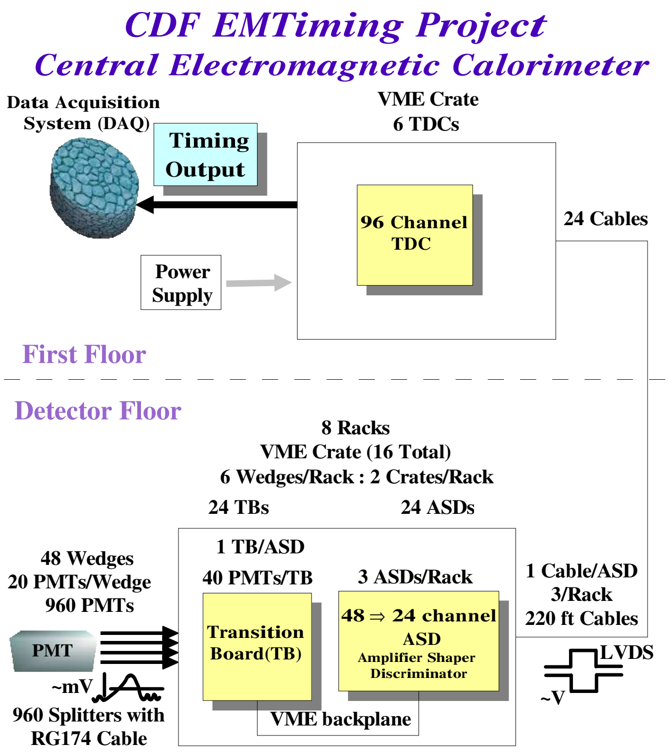

Figure 5.33: Layout of the central electromagnetic calorimeter components for the EMTiming project.

board for use in the TDC system. Figure 5.35 shows a circuit digram of the splitter and Figure 5.36 shows a photograph of a working prototype. The splitter works by inductively coupling the primary line (to the CEM ADMEM's) to the secondary output, and the grounds are not connected. The primary output loses a negligible amount of the charge which is used for the energy measurement and the secondary line only takes ≈15% of the output voltage for use to fire the ASD/TDC system.

There have been many tests of the splitter both on the test bench and on the detector itself. Figure 5.37 shows an oscilloscope picture of signals from a test bench and using a signal generator. From the figure, there is no discernable difference between the input shape and height before and after inserting a splitter into the system. Testing the splitter with an ADMEM shows that the amount of charge collected is the same for all tested energies. Figure 5.38 shows an example of the ADC counts with and without a splitter with a pulse height corresponding to of approximately 40 GeV. Figures 5.39 and 5.40 show similar results with and without a splitter for pedestal and readout values using the LED calibration system in-situ on the detector. The splitter shows no effect on the readout other than to shift the signal arrival time at the ADMEM by ≈1 nsec.

As a test of the efficiency and noise on the split signal, we find that for energies high relative to the ASD threshold that the splitter fires the ASD/TDC system with 100% efficiency at just above 1 nsec resolution, see Figure 5.41, with resolution dominated by the 1 nsec TDC resolution. There is no evidence of mis-firing[2] of the TDC or extra energy deposited into the ADMEMs from the splitter. This is shown in Figure 5.42 which shows the number of times the TDC fires around the LED firing. The full chain from CEM PMT all the way to the readout of the TDC has been established on the detector in-situ, proving that the system works as expected.

The PEM also has 960 phototubes, however those bases already have a dynode output designed into the base, so no modification is required. This system will look virtually identical to the HADTDC system except instead of having the cables soldered to the ASD transition board, we will use LEMO connectors to make cable installation easier and decoupled from

[2] We note that preliminary studies have no mis-firings in any of our LED tests. This means that at 95% C.L. there is less than a 0.1% chance in 132 nsec that the TDC will mis-fire due to spurious noise picked up by the splitter.

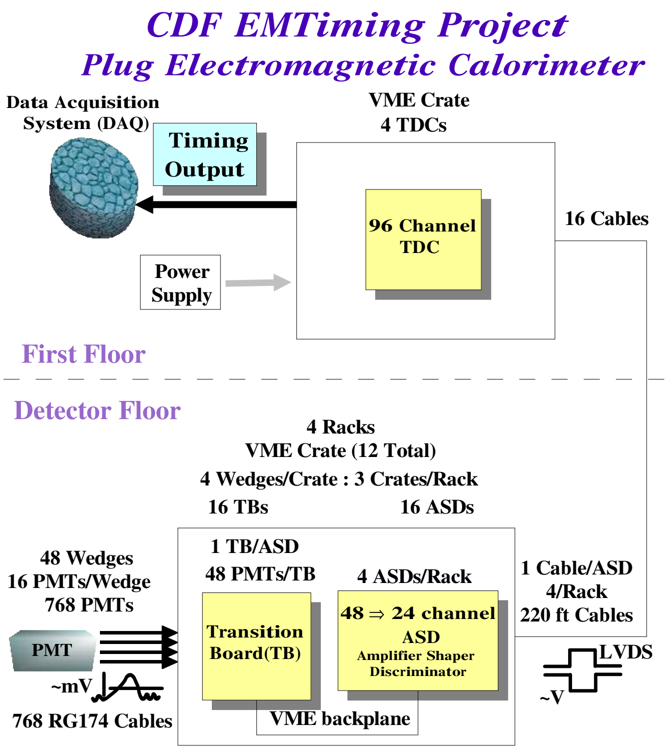

Figure 5.34: Layout of the plug electromagnetic calorimeter components for the EMTiming project.

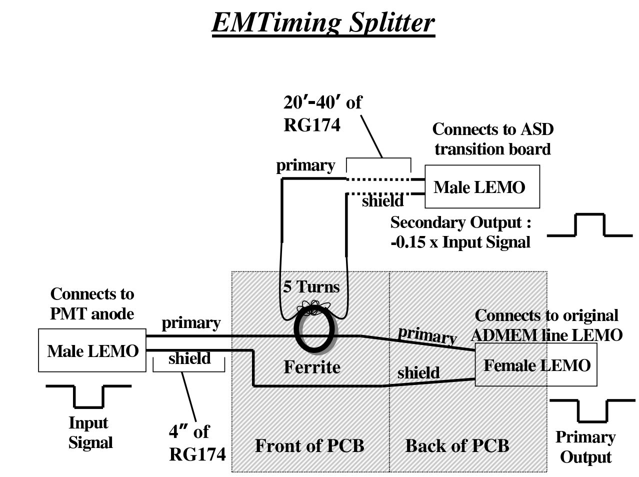

Figure 5.35: A circuit diagram of the EMTiming splitter for the central calorimeter.

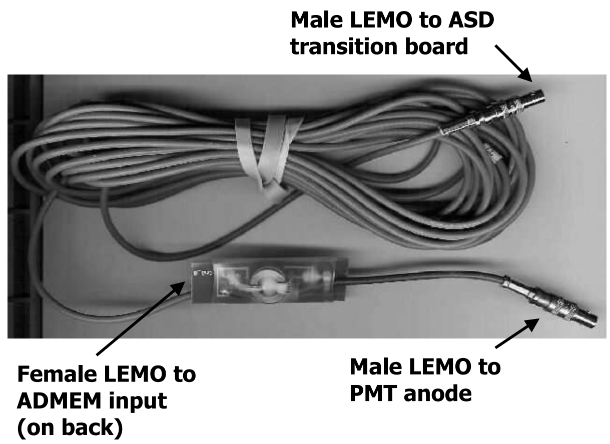

Figure 5.36: Photograph of a working prototype EMTiming splitter for the central calorimeter.

the ASD/TB installation. This will also make testing and debugging easier. We are only instrumenting the 768 towers with the smallest η as this significantly reduces the number of cables and boards in the system.

The electronics requirements are similar to those for the HADTDC system. The equipment needed includes 40 Transition boards, 40 ASD boards, 10 TDC boards, a TDC crate, and around 2000 cables. The parts are detailed in Table 5.2. No new technology needs to be researched or developed. Everything re-uses equipment or designs. Working prototypes of the splitter harness exist and in tests have functioned as expected. Prototypes of the PEM cable harness, which is simply RG174 with LEMO and AMP connectors are in progress and are following the existing designs which are currently being used in the PHATDC system. New boards with the same ASD design are being produced. New transition boards are being built with virtually identical layout to those used in the WHA except instead of 36 channels they take in 48 channels. The long cables from the ASDs on the detector floor to the TDC on the first floor are identical to those used in HADTDC system for the short stretch from the TDC patch panel to the TDC, except that they are 220 feet in length. We have chosen these cables since we do not have the same cable to cable slewing requirements in the trigger, nor the muon system routing requirements, and this allows us to use these cheaper, lighter, more flexible cables which also contain three times as many lines per cable. Prototypes of these cables have been bench-tested using the same LVDS driver/receiver chip sets on the ASD/TDC boards and the same output signals from the ASD's. Overnight tests have been shown to have 100% efficiency, adequate sample and hold times, and only add ≈25 psec of jitter to the timing resolution which is comparable to the system in use. The TDC's which are currently in the existing system are being replaced, and we are recycling 10 from the currently existing pool. The TDC

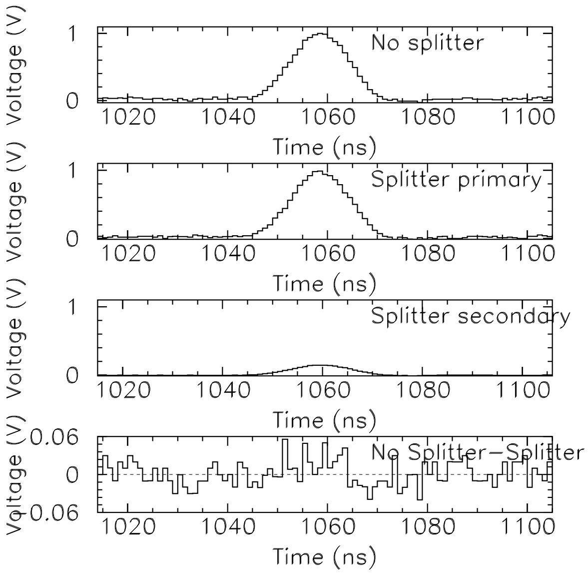

Figure 5.37: Scope results for the EMTiming splitter for a 1 volt input pulse from a signal generator. The top plot shows the generator directly into the scope. In the next plot a splitter is used and the distribution is taken from the primary output, with the secondary output shown in the following plot. The splitter and no-splitter outputs are virtually identical as shown in the difference plot which is on the bottom.

crate and Tracer will be taken from spares with the power supply and crate processor purchased off the shelf.

5.3.4.1 Work Required Prior to Start of Run IIb

There are several tasks that need to be completed before the beginning of the Run IIb shutdown. The parts for the splitters and PEM cables must be procured, and harnesses for both assembled. The transition boards and ASD's will need to be built. The ASD→TDC cables will need to be purchased. We will re-use the existing TDC boards, and the TDC crate parts will be recycled or purchased off the shelf. All the work above, including the upstairs TDC crate, can be done ahead of the Run IIb shutdown so that the only installation work that needs to be done during the shutdown is inserting the ASD/TB into the existing crates and running the cables. This will allow adequate time for testing. We note that we have many of the parts already in hand, most having been recycled, and many of the rest of the small parts are off-the-shelf items which are either in stock or have

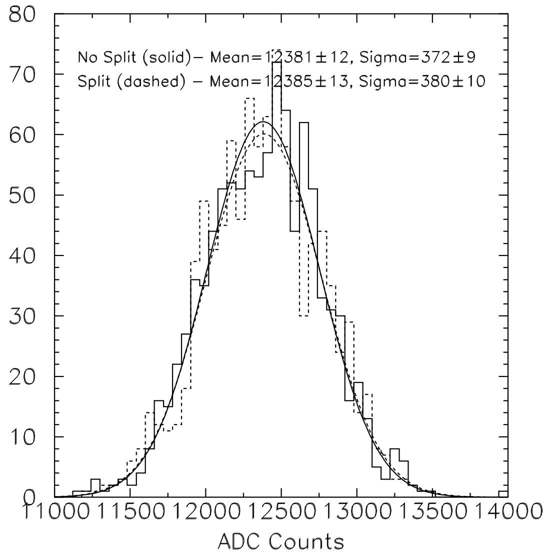

Figure 5.38: The charge deposition in the ADMEM, measured in ADC counts, with and without the EMTiming splitter for a PMT pulse corresponding to about 40 GeV on a test bench. Both the means and widths are identical within statistical errors. Similar results for other energies can be found in Ref. [2].

short lead times.

5.3.5 Summary and Conclusions

To summarize, the EMTiming project will augment the readout of the central and plug electromagnetic calorimeters for Run IIb to include timing information by adding hardware similar to that in the existing HADTDC system. This upgrade would significantly improve the potential of the CDF detector to do physics in samples with photons in the final state in two main ways: 1) It would reduce the cosmic ray backgrounds for important and difficult searches and measurements in a way which allows for significantly lower E_T^γ thresholds, larger η acceptance and with a flat efficiency as a function of E_T; 2) It would provide a vitally important handle to help confirm that all the photons in unusual events, such as the $ee\gamma\gamma\not{E}_T$ candidate event, are from the primary interaction. With sufficient calibration data, there is even the possibility of searching for very long-lived particles which decay into photons.

In Run II, even with twenty times the data, in the case that we do see a statistically significant excess of such events, it is still likely to be at relatively low statistics and we will need all the background rejection we can get. Furthermore, as in the case for the

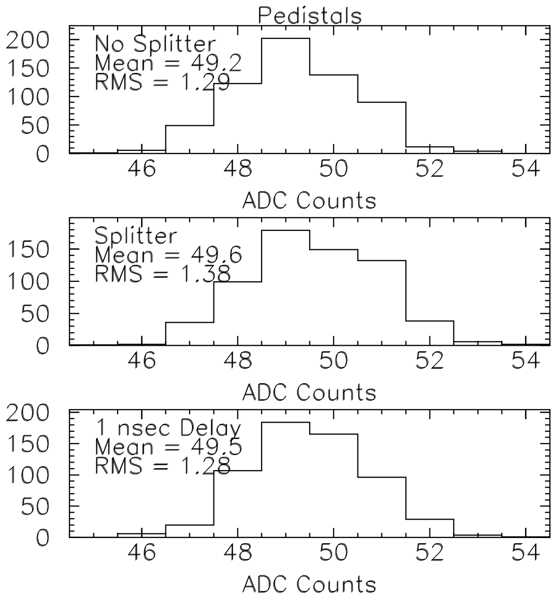

Figure 5.39: The number of ADC counts as measured by a CEM PMT/ADMEM combination on the detector using LED pedestal runs. The top plot shows the results for no splitter, the middle plot for the splitter and the bottom plot for a 1 nsec delay to take into account systems present timing window settings. As expected there are negligible differences between them.

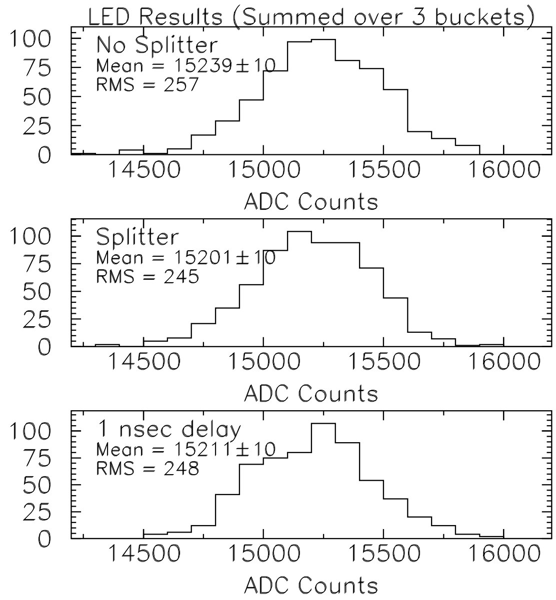

Figure 5.40: The number of ADC counts as measured by a CEM PMT/ADMEM combination on the detector using LED data runs. The top plot shows the results for no splitter, the middle plot for the splitter and the bottom plot for a 1 nsec delay to take into account systems present timing window settings. As expected there is negligible differences between them.

$ee\gamma\gamma\not\!\!E_T$ candidate event, even the most lenient critics will want to see that on a case-by-case basis any unusual events containing photons (and especially those with $\not\!\!E_T$) are not due to cosmic ray sources. In these cases, with no model to guide the experimenter on ways to verify an explanation, timing information is crucial.

We believe that the significant physics prospects provide adequate justification for this project. There is no new technology which needs to be developed so there are virtually no technical risks. Ultimately, the bottom line is that for a modest cost we can significantly extend the discovery potential for certain types of new physics.

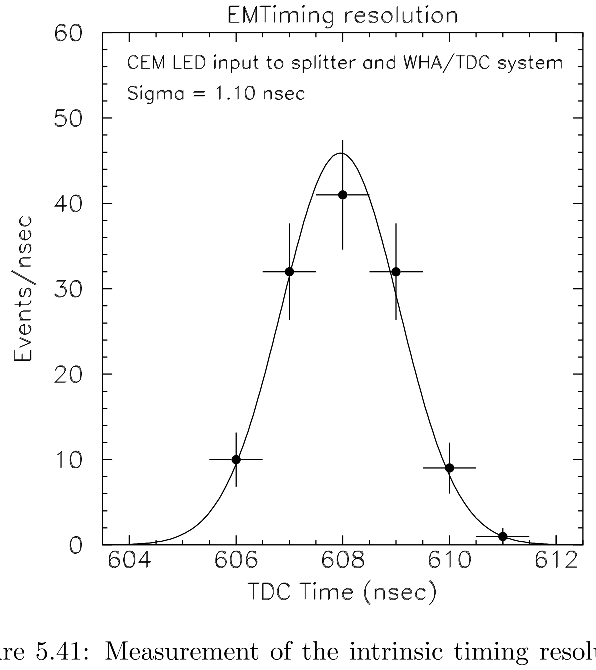

Figure 5.41: Measurement of the intrinsic timing resolution of the EMTiming System using the CEM LED's and a splitter hooked up into a WHA HAD TDC channel.

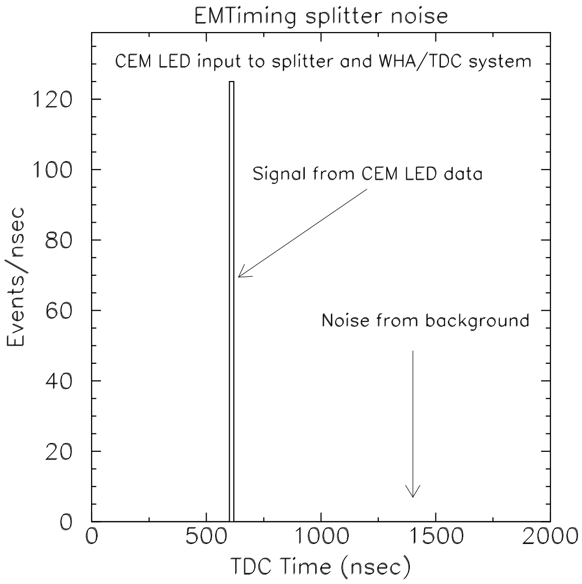

Figure 5.42: This plot shows the time of arrival distribution of the light deposited by the LED in the PMT of the CEM. We note that all the events are within about a nsec of each other, and that the TDC never fires otherwise. This shows that no noise is picked up by the splitter which might make the TDC fire.

CEM	main units	spares	Comments
Splitter Harness			
LEMO Cannon	960	96	EPL.00.250 NTN
RG174 cable	23,040ft	2,304ft	RG174→TB, ≈30 ft/cable
Male LEMOs	960	96	FFS.00.250.NTCE31
Lemo-ettes	960	96	FFS.00.250.NTCE31
Ferrite Torroid	1,200	120	Phillips TX/13/7.1/4.8-3E27
Wire, ties & shrink wrap	1	0	
Circuit boards	30	0	UC dwg A-2508, 40 splitter/board
Transition Board (TB)	24	3	
24 Channel ASD Board	24	3	
ASD→TDC cable	24	8	3M 3756/68,3M 10168-8100-EE
96 Channel TDC Board	6	1	
Crate	1		
Crate Power Supply	1		
Tracer	1		
Crate Processor	1		
PEM	main units	spares	Comments
PEM Harness			
M Lemo connectors	768	77	FFS.00.250.NTCE31
RG174 cable	17,664ft	1,766ft	RG174→TB, 23 ft/cable
Ferrule	1,000	0	AMP 1-332056-0
Socket	1,000	100	AMP 51565-1
20 pin Connector	96	10	AMP 201356-1
Housing	100	6	AMP 204087-1
Female Jackscrew Kit	100	6	AMP 200867-1
Male Jackscrew Kit	100	6	AMP 200868-1
Transition Board (TB)	16	2	
24 Channel ASD Board	16	2	
ASD→TDC cable	16	4	3M 3756/68, 3M 10168-8100-EE
96 Channel TDC Board	4	1	

Table 5.2: Parts list for the EMTiming project.

Bibliography

[1] D. Toback *et al.*, "Proposal to Add Timing Information Into the Readout of the Central and Plug Electromagnetic Calorimeters," CDF Note 5518.

[2] For more information on this project please visit
http://hepr8.physics.tamu.edu/hep/emtiming/

[3] CDF Collaboration, F. Abe *et al.*, Phys. Rev. Lett. **81**, 1791 (1998) and Phys. Rev. D. **59**, 092002 (1999); D. Toback, Ph.D. dissertation, Univ. of Chicago (1997).

[4] CDF Collaboration, D. Acosta *et al.*, Phys. Rev. Lett. **89**, 041802 (2002) and Phys. Rev. D 66, 012004 (2002). J. Berryhill, Ph.D. dissertation, Univ. of Chicago (2000).

[5] CDF Collaboration, D. Acosta *et al.*, hep-ex/0205057, submitted to Phys. Rev. Lett.

[6] CDF Collaboration, T. Affolder *et al.*, Phys. Rev. D **65**, 052006 (2002).

[7] CDF Collaboration, T. Affolder *et al.*, Phys. Rev. D. **64**, 092002 (2001).

[8] S. Ambrosanio *et al.*, Phys. Rev. Lett. **76**, 3498 (1996).

[9] S. Dimopoulos, M. Dine, S. Raby, and S. Thomas, Phys. Rev. Lett. **76**, 3494 (1996).

[10] J. L. Lopez and D. V. Nanopoulos, Mod. Phys. Lett. A **10**, 2473 (1996).

[11] For example, see S. Ambrosanio, G.L. Kane, G.D. Kribs, S. Martin, and S. Mrenna, Phys. Rev. **D** 54, 5395 (1996).

[12] B. C. Allenach, S. Lola, and K. Sridhar, Phys. Rev Lett **89**, 011801 (2002).

[13] J. L. Rosner, Phys. Rev. D. **55**, 3143 (1997).

[14] U. Baur, M. Spira, and P. M. Zerwas, Phys. Rev. D. **42** 815 (1990); E. Boos, A. Vologdin, D. Toback and J. Gaspard, Phys. Rev. **D** 66, 013011 (2002).

[15] A. D. De Rujula, M. B. Gavela, P. Hernandez, and E. Masso, Nucl. Phys. B **384**, 3 (1992).

[16] M. Baillargeon *et al.*, hep-ph/9603220 (1996).

[17] N. Arkani-Hamed, S. Dimopoulos, and G. Dvali, Phys. Lett. **B429**, 263 (1998).

[18] A. Brignole, F. Feruglio, M. L. Mangano, and F. Zwirner, Nucl. Phys. B **526**, 136 (1998); Erratum-ibid. B **582**, 759 (2000).

[19] H. Haber, G. Kane, and T. Sterling, Nucl. Phys. B **161**, 493 (1979); A. Stange, W. Marciano, and S. Willenbrock, Phys. Rev. D. **49**, 1354 (1994); M.G. Diaz and T. Weiler, hep-ph/9401259 (1994); A.G. Akeroyd, Phys. Lett. B **68**, 89 (1996).

[20] DØ Collaboration, B. Abbott *et al.*, Phys. Rev. D. **62**, 092004 (2000); DØ Collaboration, B. Abbott *et al.*, Phys. Rev. D **64**, 012004 (2001); DØ Collaboration, B. Abbott *et al.*, Phys. Rev. Lett. **86**, 3712 (2001).

[21] P. Onyisi, "Efficiency of central and wall hadron timing information for cosmic ray discrimination for Run 1," CDF Note 5460; M. Cordelli *et al.*, "Timing calibration of CDF hadron calorimeters", CDF Note 5856.

[22] D. Toback and P. Wagner, "Simulation of the Calorimeter Timing System," CDF Note 5866.

[23] S. Kuhlmann, "Timing Information For Central Photons and the ee$\gamma\gamma$MET Event," CDF Note 4256.

[24] DØ Collaboration, S. Abachi *et al.*, Phys. Rev. Lett. **78**, 3640 (1997). DØ Collaboration, S. Abachi *et al.*, Phys. Rev. D. **57**, 3817 (1998).

[25] H. Frisch, M. Goncharov, H. Sanders and D. Toback, “The CEM Timing Splitter”, CDF Note in progress. For the latest version see Ref. [2].